

*Digital Comprehensive Summaries of Uppsala Dissertations  
from the Faculty of Science and Technology 2601*

# Additive Manufacturing of Biodegradable Magnesium Alloy WE43

*Linking Process Parameters to Microstructure and  
Mechanical Performance*

LISA LARSSON



ACTA UNIVERSITATIS  
UPSALIENSIS  
2025

ISSN 1651-6214  
ISBN 978-91-513-2633-7  
urn:nbn:se:uu:diva-569726



UPPSALA  
UNIVERSITET

Dissertation presented at Uppsala University to be publicly examined in 101121, Sonja Lyttkens, Ångströmlaboratoriet, Regementsvägen 10, Uppsala, Friday, 5 December 2025 at 09:15 for the degree of Doctor of Philosophy. The examination will be conducted in English. Faculty examiner: Professor Jon Molina (IMDEA Materials Institute).

### **Abstract**

Larsson, L. 2025. Additive Manufacturing of Biodegradable Magnesium Alloy WE43. Linking Process Parameters to Microstructure and Mechanical Performance. *Digital Comprehensive Summaries of Uppsala Dissertations from the Faculty of Science and Technology* 2601. 79 pp. Uppsala: Acta Universitatis Upsaliensis. ISBN 978-91-513-2633-7.

Powder bed fusion – laser beam (PBF-LB) of magnesium (Mg) alloys, particularly WE43 (Mg-4wt%Y-3wt%RE-Zr), offers promising potential for biodegradable medical implants. This thesis investigates the influence of key process parameters in PBF-LB on the microstructure, residual stress, texture, and mechanical properties of alloy WE43 (Mg-4wt%Y-3wt%RE-Zr). This knowledge is intended to support the continued development and implementation of PBF-LB processed WE43 for applications in biodegradable medical implants. The effects of laser power, hatch distance, build size and orientation, as well as laser scan rotation, were systematically investigated.

Increased energy input through higher laser power promoted equiaxed dendritic grain formation, which enhanced tensile strength. Hatch distance could be optimized to maintain tensile properties even at lower laser powers, and influenced grain size, texture and distribution of secondary phases. Build direction had a large impact on the magnitude of the residual stresses, with larger builds in the vertical direction giving larger stress gradients throughout the sample. Tensile residual stresses were observed at the sample edges, correlating with reduced hardness in those regions compared to the bulk.

Horizontally built specimens showed approximately 40% higher tensile strength (215 MPa vs 150 MPa) and about 20% higher elastic modulus (44 GPa vs 37 GPa) than vertically built ones, primarily due to the development of a strong basal texture along the build direction. This anisotropy implies that part orientation during PBF-LB has a significant impact on performance in service. It was demonstrated that laser scan rotation significantly influences the crystallographic texture, which has the potential to affect the mechanical response of the printed parts. Rotations of 67° and 90° maintain high densification and mechanical integrity while modifying texture. Rotations of 60° and 120° further demonstrate texture control, and a segmented chessboard strategy enhances compressive strength despite weaker texture, due to favourable pore distribution and dendritic grain formation. Conversely, limiting scan rotation to 0° or 180° results in poor densification (<99% relative density), compromising structural integrity. Together, the work included in the thesis provides a comprehensive foundation for PBF-LB considerations to achieve desirable microstructural and mechanical outcomes in WE43, supporting its potential use in biomedical applications.

*Keywords:* Powder bed fusion - laser beam, additive manufacturing, magnesium, WE43, microstructure

*Lisa Larsson, Department of Materials Science and Engineering, Box 35, Uppsala University, SE-751 03 Uppsala, Sweden.*

© Lisa Larsson 2025

ISSN 1651-6214

ISBN 978-91-513-2633-7

URN urn:nbn:se:uu:diva-569726 (<http://urn.kb.se/resolve?urn=urn:nbn:se:uu:diva-569726>)

To my grandparents *in memoriam*



# List of Papers

This thesis is based on the following papers, which are referred to in the text by their Roman numerals.

- I. Nilsson Åhman, H., Larsson, L., Wahman, C., Mellin, P., D'Elia, F. & Persson, C. (2024) Higher laser power improves strength but reduces corrosion resistance of Mg WE43 processed by powder bed fusion. *Materials Today Communications*, 39:108979
- II. Nilsson Åhman, H., De Berardinis, N., Larsson, L., Rothkranz, L., Mellin, P., D'Elia, F. Hulsart, G., & Persson, C. Laser hatch distance can tune corrosion behaviour and mechanical properties while maintaining *in vitro* biocompatibility of additively manufactured Mg alloy WE43. *Manuscript*.
- III. Larsson, L., Nilsson-Åhman, H., D'Elia, F., Maimaitiyili, T., Persson, C. On the relationship between process parameters and residual stress in large WE43 builds produced by PBF-LB. *Manuscript*.
- IV. Larsson, L., D'Elia, F., Sahlberg, M., Persson, C. (2025) Leveraging laser powder bed fusion to alter texture and mechanical properties of magnesium alloy WE43. *Materials & Design*, 256:114299
- V. Larsson, L., Luzin, V., Salvemini, F., Shtender, V., D'Elia, F., Sahlberg, M., Persson, C. The role of laser scan rotation in additive manufacturing of Mg-RE alloy WE43. *Manuscript*.

Reprints were made with permission from the respective publishers.

# Author's contributions

The author's contributions to the papers included in the thesis are as follows:

- I. Formal analysis and investigation in terms of mechanical characterisation. Part in sample manufacturing. Part in visualisation of data and writing the original draft, as well as data curation.
- II. Formal analysis and investigation in terms of mechanical characterisation. Part in sample manufacturing. Part in visualisation of data, writing the original draft as well as reviewing & editing. Part of data curation.
- III. Part in conceptualisation as well as formal analysis and investigation. Performed major part of visualisation and writing original draft. Major part of data curation.
- IV. Part in conceptualisation and methodology. Performed majority of formal analysis and investigation. Performed major part of visualisation and the writing of the original draft. Major part of data curation.
- V. Part in conceptualisation and methodology. Performed part of formal analysis and investigation. Performed major part of visualisation and the writing of the original draft. Major part of data curation.

# Contents

Introduction.....	11
2 Aims and objectives.....	13
3 Background.....	14
3.1 Magnesium and its alloys in biomedical applications.....	14
3.1.1 Magnesium as a biodegradable metal.....	14
3.1.2 Crystal structure.....	16
3.1.3 Role of alloying elements.....	16
3.1.4 Alloy WE43.....	17
3.2 Powder bed fusion – laser beam.....	18
3.2.1 Working principle.....	19
3.2.2 Process parameters.....	21
3.2.3 Microstructure and texture considerations in PBF-LB builds ....	23
3.2.4 Residual stress in PBF-LB.....	26
3.2.5 Porosity in PBF-LB.....	28
3.3 Powder bed fusion-laser beam of magnesium alloy WE43.....	29
3.3.1 Microstructure and texture in PBF-LB WE43.....	29
3.3.2 Residual stress in PBF-LB WE43.....	32
3.3.3 Mechanical properties of PBF-LB WE43.....	32
3.3.4 Degradation behaviour of PBF-LB WE43.....	33
3.3.5 Biological response to PBF-LB WE43.....	34
4 Experimental methods.....	35
4.1 Powder bed fusion – Laser beam.....	35
4.2 Build quality.....	36
4.3 Microstructure characterization.....	38
4.4 Residual stress analysis.....	39
4.5 Texture analysis.....	40
4.6 Evaluation of mechanical properties.....	41
4.7 Statistical analysis.....	42
5 Summary of key results.....	43
5.1 Study I: Higher laser power improves strength but reduces corrosion resistance of Mg WE43 processed by powder bed fusion.....	43

5.2 Study II: Laser hatch distance can tune corrosion behavior and mechanical properties while maintaining <i>in vitro</i> biocompatibility of additively manufactured Mg alloy WE43 .....	45
5.3 Study III: On the relationship between process parameters and residual stress in large WE43 builds produced by PBF-LB .....	47
5.4 Study IV: Leveraging laser powder bed fusion to alter texture and mechanical properties of magnesium alloy WE43 .....	49
5.5 Study V: The role of laser scan rotation in additive manufacturing of Mg-RE alloy WE43 .....	52
6 Thesis discussion .....	55
7 Conclusions.....	61
8 Future perspectives .....	63
9 Svensk sammanfattning .....	65
10 Acknowledgements.....	66
11 References.....	69

# Abbreviations

AM	Additive manufacturing
EBS	Electron backscatter diffraction
EDX	Energy-dispersive X-ray spectroscopy
BSE	Backscatter electron
HCP	Hexagonal close packed
IPF	Inverse pole figure
LOM	Light optical microscopy
Mg	Magnesium
PBF-LB	Powder bed fusion – laser beam
RE	Rare earth
SEM	Scanning electron microscopy
SXRD	High-energy synchrotron X-ray diffraction
XRD	X-ray diffraction



# Introduction

The relationship between material processing, microstructure and properties lies at the heart of materials science and engineering. As novel processing routes for materials emerge, like additive manufacturing (AM) of magnesium (Mg) alloys has recently done, evaluating this relationship becomes essential to utilize the full potential of the new technology and enable future applications.

Mg and its alloys have attracted significant interest for biomedical applications, thanks to several valuable properties such as low density, elastic modulus close to that of bone, and excellent biodegradability. Among Mg alloys, the WE43 alloy family (Mg–Y–RE–Zr, RE=rare-earth) stands out for its high mechanical strength and good corrosion resistance, making it an excellent candidate for medical implants, as well as other lightweight applications such as in the aerospace industry. In fact, a Mg–Y–RE–Zr alloy has already been used clinically as the material for the first CE-certified biodegradable metal bone screw [1].

When it comes to AM, powder bed fusion with laser beam (PBF-LB) is a prominent technique capable of producing highly complex geometries through the selective melting of thin layers of metal powder layer by layer. This unique design freedom is particularly interesting in the biomedical field, as it allows for the design of patient-specific implants. The PBF-LB process involves high thermal gradients, rapid solidification rates, and cyclic heating, all of which lead to the formation of unique microstructures that differ significantly from those generated by conventional processing methods. Consequently, correlations between process and microstructural evolution, and resulting material properties must be re-examined in the context of PBF-LB.

The first study on PBF-LB of Mg alloy WE43 was reported in 2015 [2]. Since then, the microstructure and melt pool dynamics have been explored for certain process parameters [3]–[5]. However, the influence of key processing conditions on the resulting material features, particularly texture and residual stress, and their subsequent impact on material performance and biocompatibility remains underexplored.

The overall goal of this thesis is to deepen the understanding of how key PBF-LB process parameters influence the resulting material properties of the

WE43 Mg alloy. By linking the herein characterised microstructure, texture and residual stresses to processing conditions, this work aims to establish a framework that supports the development of reliable, biodegradable Mg components.

The aims and objectives are further outlined in section two. An introduction to Mg and its alloys, the PBF-LB process and PBF-LB of Mg is presented in section three. The experimental methods used in the thesis work are presented in section four, with the results from the five studies summarised in section five. Finally, an overarching discussion of the thesis is found in section six, followed by conclusions and future perspectives in section seven and eight, respectively.

## 2 Aims and objectives

The overall aim of this thesis is to clarify the link between important PBF-LB process parameters and the resulting microstructure, residual stress, texture, and mechanical properties of Mg alloy WE43. This knowledge is intended to support the continued development and eventual implementation of PBF-LB processed WE43 for applications in biodegradable medical implants. In alignment with this aim, the specific aim for each project and the subsequent objectives addressed in each of the included studies are as follows:

In Study I, the aim was to explore the effect of laser power, one of the main PBF-LB process parameters, as a means to tailor the energy input and associated thermal history. The resulting microstructures were characterized and linked to the alloy's tensile properties.

In Study II, the aim was to investigate the effect of hatch distance, which governs the overlap between adjacent melt pools, thereby impacting the thermal history and solidification conditions. These effects were examined in relation to microstructure and tensile properties, while assessing the corrosion properties and biocompatibility for the optimal hatch distance.

In Study III, the aim was to clarify the development of residual stress in the WE43 alloy. Building on findings from Study I and II, where the energy input and re-melting clearly impacted both microstructure and resulting properties, Study III focused on how variations in hatch distance, scan strategy and build size affects thermal gradients during solidification, which in turn govern the magnitude and spatial distribution of residual stresses.

In Study IV, the aim was to investigate the potential of tailoring the texture and mechanical performance of WE43 produced by PBF-LB, by altering the laser scan strategy and build direction. To meet this aim, the influence of common, but distinctly different, build directions and laser scan rotations was investigated in terms of texture evolution and mechanical properties of built samples.

In Study V, the objective was to build upon the texture findings from Study IV by exploring the role of laser scan rotation in tuning the texture during PBF-LB processing of WE43. A broader range of scan rotation strategies, including unidirectional and segmented approaches, was systematically investigated to evaluate their impact on grain growth and texture evolution, with the aim of improving control over the alloy's mechanical properties.

## 3 Background

In this section, an overview of Mg and its alloys is presented, followed by an introduction to PBF-LB. Finally, the work on PBF-LB of Mg alloys published thus far is summarised.

### 3.1 Magnesium and its alloys in biomedical applications

#### 3.1.1 Magnesium as a biodegradable metal

Today, the main applications for biodegradable metals involve the implantation of temporary devices such as screws, plates, pins, and stents [6]. These materials are especially valuable in bone fracture treatments, where implants provide temporary mechanical support during healing and then gradually degrade, eliminating the need for surgical removal. This can reduce long-term complications and infection risks associated with permanent implants, especially amid the growing antibiotic resistance [7], [8]. In fact, the need for suitable bone implant materials is large, as bone fractures affected an estimated 178 million individuals globally in 2019 [9].

Biodegradable metals have gradually attracted more attention as alternatives to the first-generation biomedical materials such as 316 L stainless steel and titanium alloys, as well as the second-generation<sup>1</sup> biomedical materials (i.e. bioactive glass and bone cements) [10]–[12]. Broadly, when it comes to the application of biodegradable metals as temporary implants, the most desirable properties include biocompatibility, adequate mechanical properties, natural degradability, and sufficient corrosion resistance to avoid premature degradation [13]–[15]. The most researched biodegradable alloys include those based on Mg, iron (Fe) and zinc (Zn) [13]. These materials have all been found to provide biodegradability, acceptable cytocompatibility and *in vivo* response, and relevant mechanical integrity [15]–[17]. However, they all present their own downsides. Mainly, Mg typically degrades too quickly, Zn lacks sufficient strength and ductility, and Fe typically corrodes too slowly to

---

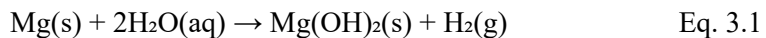
<sup>1</sup> Generations of biomaterials can be defined as first generation being bioinert, second generation being bioactive and third generation being regenerative.

be clinically effective. A full comparison of their respective properties can be found in Table 3.1.

Table 3.1. Overview of properties of the most common biodegradable metals, Mg, Fe and Zn, as well as for cortical bone [14], [18], [27]–[30], [19]–[26]. Values are given for pure metals. Tabulated values for Mg alloy WE43 are given under section 6.

	Density (g/cm <sup>3</sup> )	Young's modulus (GPa)	Yield strength (MPa)	Ultimate tensile strength (MPa)	Corrosion rate (mm/year)	Main degradation products
Mg (Pure)	1.74	44	88-126	166-220	0.75-4.4	Mg(OH) <sub>2</sub> , H <sub>2</sub> (g)
Zn (Pure)	7.14	97	18-110	30-115	0.26- 0.33	ZnO, Zn <sup>2+</sup>
Fe (Pure)	7.84	200	150	200	0.1-0.16	Fe <sub>2</sub> O <sub>3</sub> , Fe <sup>2+/3+</sup>
Bone (Cortical)	1.6-2.0	5-23	N/A	N/A	N/A	N/A

Out of these three materials, Mg was the first to be used as an implant for bone injury, already in the 1870s [31]. It wouldn't be until the 2020s however, that Mg bone implants got widespread use. As an essential element in the human body, Mg plays a role in hundreds of enzymatic processes, and its ions (Mg<sup>2+</sup>), released during degradation, are non-toxic and naturally regulated by the metabolic pathways of the body [32]. This minimizes the risk of adverse reactions or long-term accumulation, which can be a concern with iron-based implants. Furthermore, the degradation of Mg in physiological conditions, described by Eq. 3.1, leads to alkalinisation which may influence the local tissue response.



During the degradation process of Mg, hydrogen gas is generated, which can accumulate at the site of implantation and cause gas cavities that gives prolonged discomfort and disturbs the balance of blood cell parameters in the case of excessive release [33].

The mechanical properties of Mg closely match those of natural bone, reducing the risk of stress shielding and promoting better load transfer in orthopaedic applications [34]. In contrast, Zn has lower mechanical strength and degrades more slowly, while Fe, although strong, corrodes very slowly and can leave behind persistent degradation products (Table 3.1). Mg degrades at a rate that is faster than Zn and Fe, which can become an issue for the mechanical integrity of implants over time. Efforts are made to tailor the Mg

degradation rate with e.g. alloying or surface treatments to better suit specific clinical needs, increasing the adaptability for Mg as temporary implants.

### 3.1.2 Crystal structure

Besides excellent cytocompatibility, Mg exhibits other attractive properties such as its low density. In fact, pure Mg is the lightest structural metal with a density of approximately  $1.74 \text{ g/cm}^3$  (Table 3.1), about two-thirds that of aluminium [19]. This unique property has made it an attractive material in numerous industries where weight reduction is critical, such as aerospace, automotive, and electronics.

Mg crystallizes in a hexagonal close packed (HCP) structure which significantly influences the mechanical properties. The deformation of Mg alloys is generally limited due to their few slip systems at room temperature (see Fig. 3.1), since it only has one close packed plane (i.e. the basal plane) [35]. This makes Mg typically brittle and often results in mechanical anisotropy [36], which can be a limiting factor for their use in certain applications.

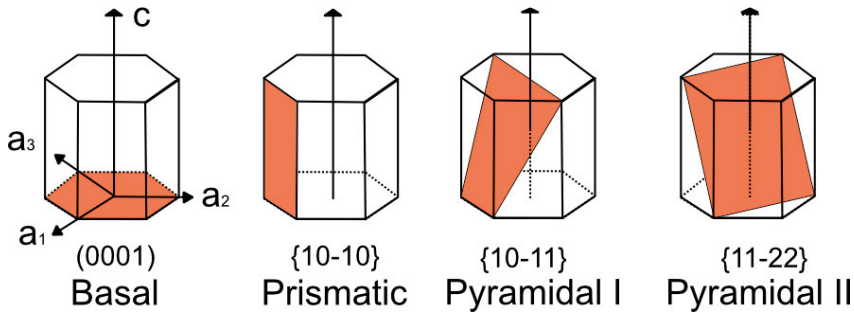


Figure 3.1. HCP crystal structure and the available slip systems for Mg. Here, the four-index Miller-Bravais notation (hkil) is used. The four-index system can be obtained from the three-index system through:  $h = h'$ ,  $k = k'$ ,  $i = -(h' + k')$ , and  $l = l'$ , where (h'k'l') are the indices from the original three-index system. Image adapted from [37], licenced under CC BY 4.0.

### 3.1.3 Role of alloying elements

The biomedical applications of unalloyed Mg are mainly constrained by its high chemical reactivity and rapid degradation (see Table 3.1), as its mechanical integrity tends to diminish almost before the surrounding tissues are fully healed [38]. To address these limitations, a wide range of Mg alloys have been developed. These typically incorporate elements such as aluminum (Al), zinc (Zn), manganese (Mn), rare earth (RE) metals, and calcium (Ca) to enhance material properties [39]. For instance, the AZ-series alloys (e.g., AZ31, AZ91)

combine aluminum and zinc to improve strength and castability, while rare-earth-containing alloys like WE43 offer superior high-temperature stability and corrosion resistance [39]. The group of AZ alloys with Al and Zn as the main alloying elements has been widely studied for potential biomedical applications. However, the biocompatibility of some of the alloying elements, in particular Al, has received severe criticism, including arguments that long-term exposure to Al could affect reproductive ability, induce dementia and cause Alzheimers disease [40], [41]. For biomedical applications, these adverse effects need to be avoided. Hence, Mg alloys containing RE elements have been proposed as good contenders as they do not only possess all of the benefits available from the existing Mg alloys in terms of biocompatibility and a Young’s modulus close to bone, but also have improved mechanical properties and corrosion resistance due to the addition of rare earth elements.

### 3.1.4 Alloy WE43

Mg-alloys belonging to the WE43 family (Mg-4wt%Y-3wt%RE-0.5wt%Zr) were the first to be approved for use for orthopedic applications (Magnezix® from Syntellix in 2013) [31]. Since then, a number of Mg-RE alloys have emerged. An overview of commercially available Mg-RE implants and their applications is found in Table 3.2.

Table 3.2. Some commercially available Mg implants and their applications.

Implant name	Composition	Application	Manufacturer	Year of approval
Magmaris®	WE43	Cardiovascular stent	Biotronik Ag, Switzerland	2016 [42]
Resoloy®	Mg-10Dy-1Nd-1Zn-0.2Zr	Cardiovascular stent	MeKo Laser Material Processing, Germany	2015 [43]
Magnezix®	MgYREZr	Ortopeadic (screw, nail, anchor)	Syntellix AG, Hannover, Germany	2013 [44]
mm.X	Mg-RE, Mg-Ca-Zn	Sports medicine (Suture anchor systems, screws)	medical magnesium, Aachen, Germany	2020 [45]

The WE43 alloy was first developed as a high strength casting alloy. The RE additions – typically neodymium (Nd) – improve the strength of the material through solid solution and precipitation strengthening, while zirconium (Zr) and yttrium (Y) are added to refine the grain size, which further improves the mechanical strength [46], [47]. Y additions also have positive effects on the corrosion properties, which is the key reason for its addition [48], [49]. Y

becomes enriched in the surface oxide layer, forming primarily yttrium oxide ( $Y_2O_3$ ), which improves passivation. However, even if the addition of alloying elements can aid the corrosion resistance of WE43, they can also lead to the precipitation of intermetallic phases that can have a detrimental effect on the corrosion performance. These intermetallic phases may act as cathodic sites relative to the Mg matrix, promoting localized galvanic corrosion and accelerating material degradation in physiological environments[50].

To improve the corrosion resistance even further than by alloy design, surface modification methods such as coating technologies have been proposed. In fact, surface coatings have been shown to significantly decrease the degradation rate of Mg alloys. Ibrahim et al. reported that a ceramic coating produced by micro arc oxidation (MAO) on a heat-treated Mg-Zn-Ca-Mn alloy resulted in a significant reduction in the corrosion rate from 10.37 mm/yr for the uncoated alloy to 0.03 mm/yr after coating *in vivo* [51].

As Mg alloy WE43 was originally developed for casting, investigating how the material behaves both in terms of mechanical integrity and during degradation when manufactured through other processing routes is essential. Overall, the development of Mg and its alloys continue to be an expanding field of research, driven by the global demand for lightweight, high-performing materials for the biomedical sector.

### 3.2 Powder bed fusion – laser beam

AM is defined as “the process of joining materials to make objects from three-dimensional model data, usually layer upon layer” according to ASTM F42 [52]. There are various AM techniques used, which can be divided into seven subcategories according to the ISO standard [53]. Out of these seven, four techniques are applicable to metal AM (Fig. 3.2) [54], [55].

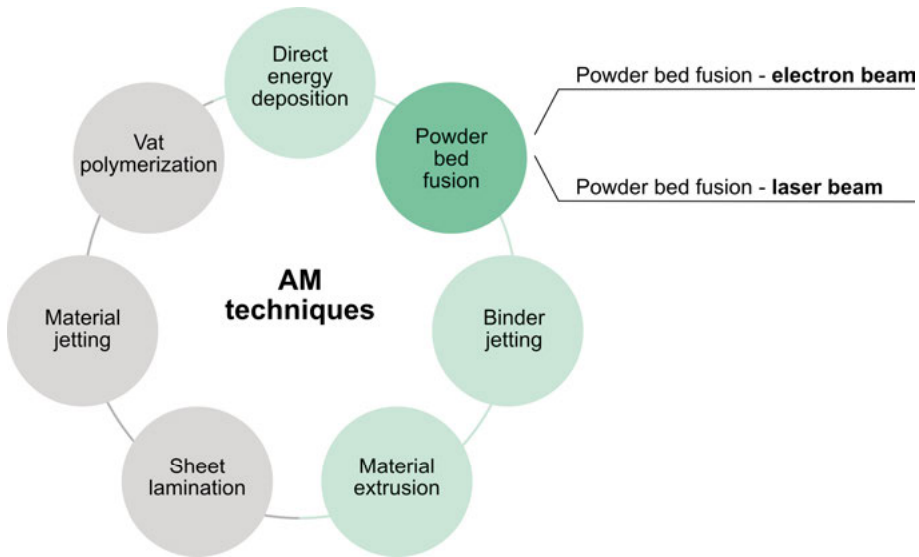


Figure 3.2. Overview of AM techniques. Techniques marked in green are suitable for metal AM. Dark green indicates PBF, which is the focus of this thesis.

As described briefly in Fig. 3.2, PBF-LB is a layer-by-layer AM technique suitable for the medical industry because of its high resolution, especially compared to electron beam melting technologies. During PBF-LB, a computer-aided design (CAD) file is used to guide the scanning of a high-power laser source to fuse powder material in order to construct a three-dimensional object. This advanced manufacturing technique has opened up new possibilities in the medical industry, allowing the manufacturing of parts with complex geometries at a relatively low unit cost. This design freedom means that customized parts can be produced in a relatively straightforward manner: complex shapes resembling the damaged part can be produced using computed tomography (CT) data, allowing for patient-specific implants [56]. Complex internal structures with controlled or graded porosities, mimicking the natural bone structure, can also be produced by AM [57]–[59]. This approach ensures the right distribution of stiffness and strength across various regions, which are virtually impossible to prepare by any traditional manufacturing method.

### 3.2.1 Working principle

The working principle of PBF-LB can be described as follows. Metal powder is distributed from a powder dispenser and evenly spread across the build platform using a roller or blade. The optimal thickness of each powder layer depends on the specific material and processing conditions, but typical values range from 20–100  $\mu\text{m}$  [60]. This thickness range is chosen as a balance

between achieving fine resolution and allowing for good powder flowability [61].

A focused laser-beam then locally melts the powder at a specific volume according to a predetermined geometry. The wavelength of the laser is for most systems in the infrared range, and most systems operate with continuous-wave lasers. Research with pulsed lasers, however, has demonstrated potential benefits. In particular, the tendency of molten metal to form disconnected balls of molten metal, rather than a flat molten region on a powder bed surface, can be partially overcome by pulsed energy [62].

After the scan, the melted zone rapidly solidifies generating the first layer and the next powder layer is deposited and melted. The area melted by the laser is denoted as the ‘melt pool’. This cycle is repeated until the part is fully fabricated. The un-fused powder around the finished object can be collected after the finished build and re-used after sieving.

In terms of spatial resolution, AM machines generally operate with a resolution of a few tens of  $\mu\text{m}$ , where PBF-LB can produce minimum features as small as  $100\ \mu\text{m}$  [60]. It is common for AM machines to also have different resolution along different orthogonal axes. Typically, the vertical build axis corresponds to layer thickness and this would be of a lower resolution compared with the two axes in the build plane [63].

A schematic illustrating the main components of the PBF-LB process can be found in Figure 3.3. The quality and properties of components produced by PBF-LB strongly depend on process parameters such as laser power, scan speed, hatch distance, and layer thickness, which all together defines the thermal history and solidification behaviour.

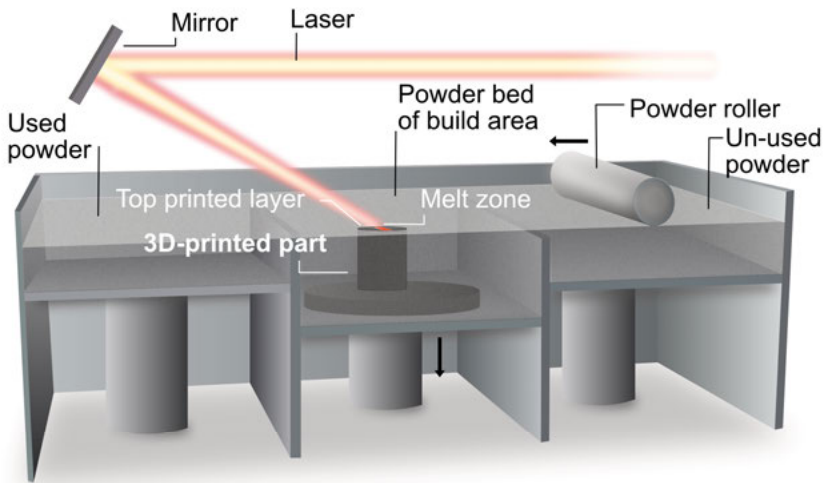


Figure 3.3. Simplified schematic of the powder bed fusion process.

### 3.2.2 Process parameters

Additively produced metal parts show a distinct microstructure which can be strongly influenced and tailored by the process parameters. There are numerous process parameters that can be varied during the PBF-LB process, the main ones (illustrated in Figure 3.4) include laser power ( $P$ ), laser scan speed ( $v$ ), beam spot size, hatch distance and scan strategy. The process parameters most relevant for the thesis are further outlined below.

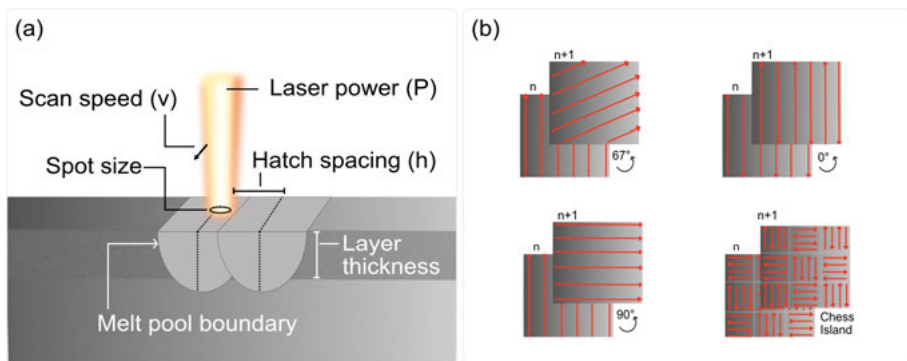


Figure 3.4. Schematic view of process parameters relevant during the PBF-LB process. (b) Common laser scan strategies, shown for two consecutively scanned layers ( $n$  and  $n+1$ ).

**Laser parameters** have a large impact on the final material quality after printing. Laser power, for example, impacts the energy input, with a higher power leading to deeper and wider melt pools that promote better fusion between layers and particles. However, there is a risk of defects with excessively high laser power, further outlined in section 3.2.5. The same is true for insufficient laser power, which e.g. may result in porosity due to incomplete melting. Therefore, optimizing laser power is crucial to achieving a stable melt pool and high-quality builds.

In fact, process parameter optimization is essential for PBF-LB to ensure the production of reliable and cost-effective components. By systematically optimizing the parameters shown in Fig. 3.4, defects can be significantly reduced while improving material performance. The notion of ‘energy density’ can be useful for comparing different parameter sets during process parameter optimization [64]. The volumetric energy density input can be calculated according to Eq. 1, in which P is the laser power, v the laser scan speed, t the layer thickness and h is the hatch distance. All parameters mentioned in Eq. 2 are illustrated in Fig. 3.4.

$$ED_V = \frac{P}{v \times t \times h} \quad \text{Eq. 1}$$

This equation establishes that e.g., operating at lower laser powers requires the use of lower scan speeds or smaller hatch distance in order to ensure the same energy density during the process. In addition to optimizing the laser parameters for the bulk material, which are optimized for e.g. internal density, another set of laser parameters can be optimized for ‘contour’ scans. These are parameters specifically tuned to improve surface finish.

**Hatch distance**, or the scan spacing, should be selected to ensure a sufficient degree of melt pool overlap. A smaller hatch distance ensures better overlap between melt tracks for the same laser spot size (the spot size is often fixed in a specific system), promoting uniform fusion and reducing porosity. However, if the hatch distance is too small, it can lead to excessive energy input (Eq. 1), causing overheating or distortion. On the other hand, a larger hatch distance may result in lack of fusion between tracks.

Another important factor for the build quality is the layer thickness, also shown in Fig. 4. The layer thickness is the downwards displacement of the build plate before reapplication of a new layer of powder. It often varies between 20-100  $\mu\text{m}$  [60].

**Laser scan strategy** is another important factor for the PBF-LB process. It is commonly used to describe the movement of the laser with respect to the powder bed. These scan strategies can be pre-set on the PBF system by the manufacturer or can be freely changed by the user. The most common laser scan strategy is a rotation of the laser scan direction by  $67^\circ$  between each consecutively scanned layer. This rotation is chosen to achieve the highest number of layers until returning to the original scan direction (360 layers) and can reduce residual stresses in the material [65]. A schematic of commonly employed laser scan strategies for PBF-LB is found in Figure 4b. Moreover, the choice of laser scan strategy has been shown to provide texture control in PBF-LB materials [66]

### 3.2.3 Microstructure and texture considerations in PBF-LB builds

Microstructure formation during PBF-LB is highly complex, as it is impacted by a combination of process parameters, material characteristics, and thermal conditions. One of these is the presence of oxides in the feedstock powder, making it difficult to avoid oxide inclusions in the final printed material. Powder re-use can further increase the oxygen content, which can lead to localized oxygen enrichment even though the main microstructure characteristics are similar. This can negatively affect the ductility of the printed material [67], [68].

Another factor inherent to the PBF-LB process that impacts the microstructure is the localized and directional nature of the laser heat source. This leads to steep thermal gradients and directional solidification. The local thermal conditions, and thus also the microstructure, observed in PBF-LB alloys are often similar to those observed in laser welding. In most instances in laser melting processes, solidification typically initiates from the boundary of the melt pool and progresses inwardly, towards the centre of the melt pool itself [69], [70]. This is based on the theory of directional solidification, which is defined by the temperature gradient at the solid–liquid interface ( $G$ ), typically measured in K/mm, and the growth rate of the solidification front ( $R$ ), expressed in mm/s. Their product represents the cooling rate within the solidification range, which directly influences the microstructure. Generally, higher cooling rates lead to finer microstructures and lower cooling rates lead to coarser microstructures. The  $G/R$  ratio influences the grain morphology, as described in Figure 3.5, where the solidification front tends to evolve sequentially from planar to columnar cells, to columnar dendrites, and finally to equiaxed dendrites as  $G/R$  decreases [71].

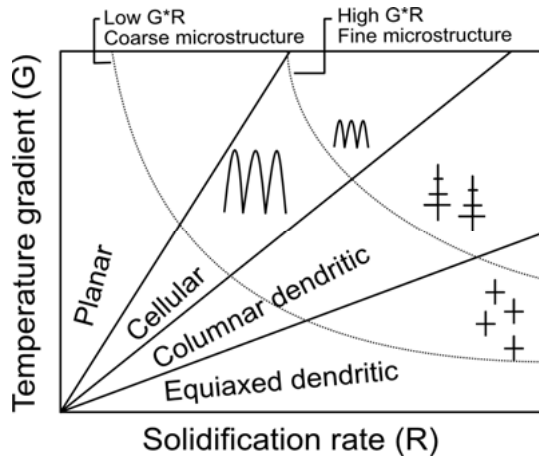


Figure 3.5. Schematic of the relation between temperature gradient ( $G$ ) and growth rate ( $R$ ) on the morphology of solidified material, adapted from [71].

Additionally, the cyclic nature of the repeated melting and solidification layer after layer also has a big influence on the microstructure and grain growth across layers. Each new layer introduces localized thermal cycles that not only re-melt portions of the previously solidified material but also create heat-affected zones (HAZ) in adjacent regions. These thermal fluctuations lead to complex interactions between solidification fronts and existing microstructures, often resulting in heterogeneous grain orientations, varying grain sizes, and potential epitaxial grain growth from one layer to the next. The repeated exposure to heat can also cause grain coarsening or refinement depending on the cooling rates and thermal gradients involved. These re-melted and heat-affected zones, which are critical to understanding the final material properties, are illustrated in Figure 3.6.

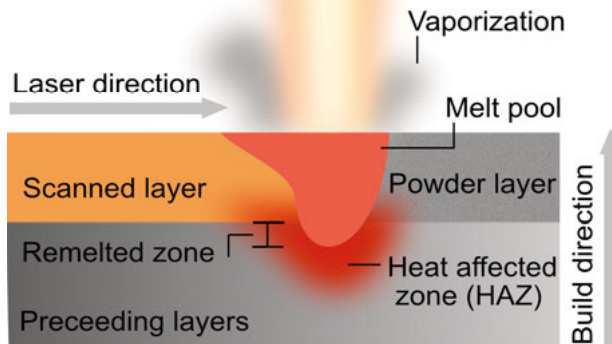


Figure 3.6. A schematic presentation of the areas surrounding the melt pool during printing, adapted based on [72], licenced under CC BY 4.0.

Most metallic materials are polycrystalline, i.e., consist of an aggregate of many crystals. Some of the properties of single crystals are directionally dependent, thus, the properties of polycrystalline materials are determined by the average orientation of the crystals (known as texture or preferential orientation). Figure 3.7 illustrates the concepts of weak and strong texture, i.e., random, and similar orientation of the crystals in a component, respectively. Depending on the alloy system, a strong crystallographic texture is formed during PBF-LB. A strong preferred orientation can translate into directional dependence of the properties, i.e., anisotropy. The mechanical properties of metals produced by PBF-LB are, in fact, often highly anisotropic [73], [74] because of the main direction of heat extraction is in the build direction. Process optimization often seeks to promote the formation of equiaxed grains, as these improve mechanical properties and reduce anisotropy.

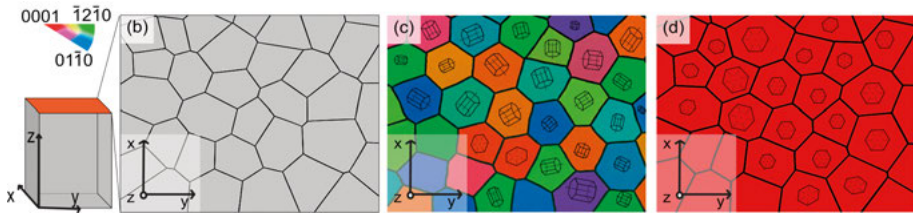


Figure 3.7. (a) represents a cubic sample and the corresponding crystallographic grains in cross-section  $xy$  (orange) of the same. The mock-up EBSD images then represents (c) weak texture (random orientation of the crystalline structure at each grain) and (d) strong texture (high degree of alignment of crystallographic orientations among grains). In both the mock-up EBSD images, the IPF colour is set to represent the crystallographic direction in the  $xy$ -plane, meaning that the red colour corresponds to a crystal orientation of  $0001$  in the  $z$ -direction.

### 3.2.4 Residual stress in PBF-LB

As presented in section 3.2.2, PBF-LB gives a vast choice in terms of process parameters. Small changes in these parameters can have significant and sometimes detrimental effects on the printed components. A wrong choice of laser parameters can cause build-up of residual stress. Understanding the origins, mechanisms and effects of these stresses is essential for optimizing PBF-LB produced material and ensuring consistent, high-quality production.

In fact, residual stress in the final built material is a well-known phenomenon when working with PBF-LB. Residual stresses are defined as stresses that remain in the material after the PBF-LB process is done. In general, residual stress formation during PBF-LB is common, due to the localized laser beam heating in combination with the high cooling rates (in the order of  $10^4$ - $10^7$  K/s [75], [76]), leading to steep thermal gradients within the built specimens. The magnitude of such residual stresses is usually large, at times even approaching the material's yield strength. If large enough, the residual stresses can cause distortion or cracking of the final component, or even delamination of the component from the build plate. Residual stresses are usually classified as Type I, Type II or Type III, depending on at which length scale they operate [77]. Type I residual stresses are macroscopic stresses that act on the scale of the component geometry and can cause distortion or warping of the built piece. Type II residual stresses occur at the grain or phase level, which mostly caused by thermal expansion mismatch between different microstructural constituents, such as precipitates and the matrix. Type III residual stresses act on even finer scale, at the atomic or sub-grain scale, and it originating from lattice distortions and dislocation structures introduced during rapid solidification. In this thesis, the discussion centres on residual stress of Type I.

In PBF-LB, residual stress mainly arises from the large thermal gradients and constrained shrinkage. Localized heating from the laser and rapid cooling create strong temperature gradients both vertically in the build direction, as well as in the build plane. When a new layer is deposited over a cooler, solidified layer, cooling and shrinkage cause tensile stresses in the new layer and balancing compressive stresses in the underlying layer. Differential cooling in the build plane intensifies stress variations due to faster cooling at the edges than in the centre. As more layers are built, stress distribution evolves, with compressive stresses accumulating in the bulk and tensile stresses near the surface [78]–[80].

The process parameters have a large impact on the resulting residual stress. A summary of the general influence of certain process parameters on residual stress formation during PBF-LB is outlined in Table 3.3. The underlying mechanisms of the observations presented in Table 3.3 that are most relevant to this thesis are further outlined in the following paragraphs.

Table 3.3. Summary of the general effect of various process considerations on the residual stress formation in PBF-LB.

Parameter change	General effect on residual stresses
Increased scan speed	Lower residual stress
Increased scan power	Higher residual stress
Re-scan/Pre-scan	Lower residual stress
Pre-heating the build plate	Lower residual stress
Scan rotation	Has an effect on RS
Shorter scan vector length	Lower residual stress
Increased hatch distance	Lower residual stress

In terms of laser power, an increase thereof tends to result in increased residual stresses. Bian et al. investigated the effect of laser power on residual stress in 316L steel by XRD, and showed that regardless of the scanning strategy, the increase of laser power from 160 W to 200 W generally leads to an increase of tensile residual stress in the area of interest (0.7 – 2 mm depth from the surface) [81]. This increase was attributed to the higher peak temperatures generated at the elevated laser power, which in turn induced steeper thermal gradients and greater thermal contraction during cooling.

An increase in hatch distance generally results in lower residual stresses in the component, as shown e.g. by Tsai et al. for 316L steel [82]. The lower residual stresses observed at larger hatch distances were attributed to the smaller overlap between adjacent melt pools. This reduced overlap minimizes localized heat accumulation and consequently lowers thermal gradients.

Lower thermal gradients, in turn, reduce the magnitude of thermally induced residual stresses by decreasing contraction between successive layers.

In terms of laser scan rotation, unidirectional scanning typically generates the highest residual stresses, particularly aligned parallel to the scan direction. Alternating scan strategies (such as  $90^\circ$  or  $67^\circ$  rotation between layers) result in more isotropic stress distributions and generally lower residual stress values [65]. In addition, the scan vector length can significantly reduce residual stresses. Extended scan vectors facilitate cooling of previously scanned regions as the laser travels longer distances, thus creating significant temperature differentials between scanned areas and new scan lines, generating higher thermal stresses. In fact, chessboard laser scan patterns have been shown to reduce residual stress compared to unidirectional approaches [83].

### 3.2.5 Porosity in PBF-LB

Porosity is another factor apart from residual stress that can negatively impact the quality of the built material. Porosity can form due to a range of factors, including insufficient energy input, improper scanning strategies, or gas entrapment. A primary source of porosity-related defects in parts fabricated by PBF-LB is improper choice of laser power and speed, which is why identifying an optimal process window (illustrated as the green area in Figure 3.8) for these parameters is a key aspect of process optimization. As seen in Figure 3.8, lack-of-fusion porosity can be caused by low laser power and/or high scan speed, leading to insufficient energy input and poor melting between layers or tracks. Keyholing, on the other hand, generally occurs at high laser power and low scan speeds, where excessive energy causes material evaporation, leading to the development of vapor cavities. The deep and unstable melt pools, resulting from the high energy input, can collapse during solidification, leading to the formation of keyhole-induced porosity.

In addition, the use of high scan speeds together with high laser powers can cause balling, which is a defect characterized by the formation of small, spherical droplets of molten material along the scan tracks, instead of smooth, continuous melt lines.

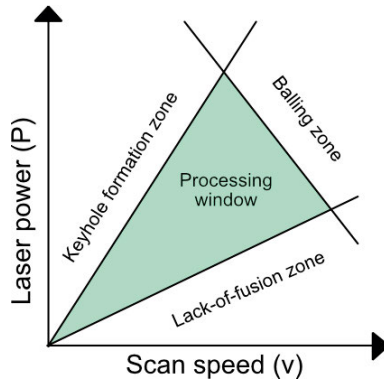


Figure 3.8. Common defects in PBF-LB components, as a function of scan speed and laser power.

### 3.3 Powder bed fusion-laser beam of magnesium alloy WE43

A number of conventional alloys with varying crystal structures have been extensively investigated for PBF-LB. These include austenitic stainless steel (316L), titanium alloys (Ti64AlV) and nickel-based superalloy (Inconel 718) [84]–[86]. Tailored compositions of conventional alloys suited for PBF-LB are also being studied [87], [88]. In contrast, Mg alloys are some of the least developed for PBF-LB, partly because of safety concerns related to the powder handling and partly because of the slim processing window for PBF-LB. Indeed, an intrinsic factor distinctive for the PBF-LB process of Mg alloys is the visible evaporation during the process, resulting from the low boiling point (1093 °C) of Mg in combination with the need for enough energy input to break the oxide layer on the Mg powder, which on the contrary has a high melting point (2852 °C) [89].

So far, investigations on PBF-LB have been performed for e.g., AZ-[90], [91], ZK- [92], and RE-based alloys [93], [94] with the WE43 alloy being the most widely studied [95], [96]. In fact, the first study on PBF-LB of Mg alloy WE43 was reported in 2015 [2]. This has opened up new possibilities for the use of biodegradable Mg in the medical industry, allowing the manufacturing of parts with complex geometries and patient specific implants [97], [98]. To date, there is no Mg implant produced by PBF-LB available on the market.

#### 3.3.1 Microstructure and texture in PBF-LB WE43

The microstructure of WE43 Mg alloy produced by PBF-LB is distinctly different to that of conventionally manufactured WE43 (e.g. via extrusion or

casting). In its as-cast state, the WE43 alloy typically exhibits relatively coarse grains due to slow cooling rates and uniform thermal history. The average grain size is often between 25–55  $\mu\text{m}$  [94], [99], [100]. PBF-LB microstructure is, however, generally characterized by a fine cellular morphology resulting from the rapid solidification rates inherent to the process, together with a high thermal gradient between the melt pool and surrounding material and powder. This is consistent with classical solidification theory, where high cooling rates suppress the growth of dendrites and favour cellular structures (see Figure 3.5 in section 3.2.3). Average grain sizes ranging from  $1.0 \pm 0.4 \mu\text{m}$  to 36  $\mu\text{m}$  have been reported [94], [101].

Nilsson-Åhman et al. investigated the microstructure of a WE43 alloy manufactured by PBF-LB compared to the microstructure of an extruded counterpart [102], and the observed differences are visualized in Figure 3.9. As seen from the image, the melt pool boundaries are clearly visible in the microstructure for the PBF-LB produced material. Furthermore, the presence of dendrites is clear. This is common for WE43 produced by PBF-LB, as the thermal conditions in PBF-LB are not constant throughout the build. In fact, the presence of dendritic morphologies has been observed in multiple studies of PBF-LB of WE43 [102], [103]. Within the melt pool itself, Bär et al. identified a lamellar zone localized at the bottom and an equiaxed zone extending from the centre to the top [5]. This reflects the thermal gradients and solidification rates throughout the melt pool during PBF-LB. In fact, D’Elia et al. demonstrated that thermal gradients during the PBF-LB process significantly influence grain morphology: steep gradients promote cellular grain structures, while shallow gradients favour dendritic growth [104].

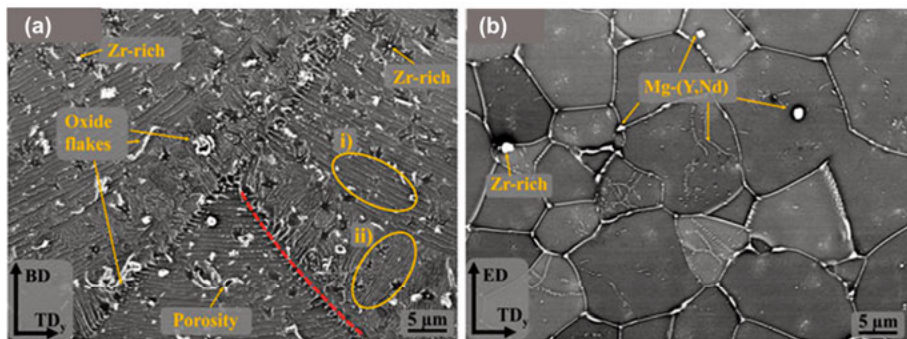


Figure 3.9. BSE-SEM images of (a) As-built WE43 produced by PBF-LB compared to (b) extruded WE43 material. (i) highlights a cellular structure that can be seen inside the melt pool and (ii) dendritic structures. Adapted from [102] licensed under CC BY 4.0.

Another key aspect of the microstructure in WE43 alloys produced via PBF-LB is the presence of intermetallic phases. These typically include  $\text{RMg}_3$  compounds (where  $R = \text{Y, Gd, Nd}$ ), oxide flakes, and Zr-rich precipitates. Bär et al. [5] identified both platelet-shaped  $\text{Mg}_{41}\text{Nd}_5$  and globular  $\text{Mg}_3\text{Nd}$  intermetallic particles in PBF-LB processed WE43. Notably, these phases tend to appear more prominently in additively manufactured material compared to conventionally processed counterparts, as illustrated by the light regions in Fig. 3.9 [102]. When compared to cast WE43, material produced by PBF-LB showed larger size and spatial distribution. This increased presence of intermetallic phases can be attributed to the localized evaporation of Mg during the laser melting, but also because of the oxide layers present at the powder surface. These surface oxides are difficult to eliminate during the PBF-LB process, making their occurrence in the final microstructure likely.

Another factor influencing the microstructure of WE43 during PBF-LB, that is not related to the process parameter selection, is alterations of the powder composition. In one study, Yin et al. provided an insight into the importance of powder composition in PBF-LB of WE43 as a means to control grain size, where they reported that a lower amount of Nd and Zr (1.98 wt% and 0.07 wt% respectively) in the powder composition lead to coarser columnar grains whilst high Nd and Zr content (2.45 wt% and 0.40 wt% respectively) significantly reduced grain size and resulted in fine equiaxed grains [105]. The fact that minor changes of alloying elements had a large impact on the grain growth (and resulting properties) highlights the need for a compositional standard of WE43 powder meant for PBF-LB to ensure reliable and repeatable results.

In terms of texture, conventionally processed RE-containing Mg alloys, e.g. produced by extrusion or casting, typically exhibit a weakened basal texture, often referred to as “RE texture.” This texture is commonly characterized by a random distribution of grain orientations and/or a tilting of basal poles away from the normal direction [106], [107]. However, this behavior is not observed in RE-containing WE43 alloys processed by PBF-LB, where grain growth is strongly influenced by the build direction [5], [101], [108]. A strong basal texture in the build direction is typically observed, i.e. the [0001] basal plane of the HCP structure being preferentially aligned perpendicular to the build direction. This texture arises due to epitaxial grain growth from previously solidified layers and the steep thermal gradients that promote directional solidification. Given the sensitivity of texture to local thermal conditions, it is essential to investigate how the different laser settings influence the evolution of crystallographic texture during PBF-LB processing, as a means to control the anisotropy which can affect mechanical properties.

### 3.3.2 Residual stress in PBF-LB WE43

To ensure dimensionally stable and defect-free builds, characterising the residual stress of PBF-LB components printed by WE43 is crucial. Residual stress measurements of biodegradable metals with intended use as degradable implants is particularly important, as built-up residual stress can negatively affect the degradation of metallic parts is the presence of residual stresses built up in the material during processing [109]. Although research on residual stress in PBF-LB WE43 remains limited, Yan et al. offered valuable insights through a three-dimensional finite element (FE) model, showing that scan strategy plays a key role in stress distribution [110]. Notably, changing the start point each circulation over the build surface produced the lowest levels of stress overall. Furthermore, Utyaganova et al. recently presented the first experimental study on residual stresses in PBF-LB of WE43 [111], however with only one measured site per print condition. Residual compressive stresses (Type I) were formed in the as-printed alloy along the printing direction with maximum values reaching  $-182$  MPa. To build a more comprehensive understanding of residual stress evolution in PBF-LB processed WE43, experimental data on the residual stress at multiple locations throughout the printed samples are needed, as well as in larger-scale builds. This will enable a more accurate assessment of stress distributions and their implications for component performance.

The finding of compressive stresses is indeed interesting, as Sealy et al. Managed to introduce compressive stresses in the surface layers of printed WE43 through a hybrid AM process, thus decreasing local corrosion by 57% [93]. However, in the case of degradable Mg alloys, these compressive surface stresses may only impede corrosion for a while, and the corrosion would increase once the compressive stress/strain layer is removed (i.e. degraded) since there is always a balancing tensile region underneath. Thus, accurately characterising the residual stress formed in Mg-alloys produced by PBF-LB is crucial for understanding and controlling the degradation behaviour of future biodegradable Mg-based implants.

### 3.3.3 Mechanical properties of PBF-LB WE43

The mechanical performance of WE43 produced by laser powder bed fusion (PBF-LB) is strongly governed by the solidification-induced microstructure. Early work by Zumdick et al. [94] provided a direct comparison between PBF-LB, conventional casting, and powder extrusion. Due to the high cooling rates inherent to PBF-LB, the as-built material exhibited a refined grain structure comparable to that of the powder-extruded condition and, consequently,

similar strength. However, the extruded alloy demonstrated higher ductility, attributed to its more homogeneous microstructure and reduced porosity, while the coarse-grained as-cast alloy showed the lowest strength and ductility among the three processing routes. Further highlighting the effect of the fine PBF-LB microstructure on mechanical strength, Xu et al. [112] reported the highest tensile properties for PBF-LB WE43 to date, with a yield strength of  $276 \pm 1$  MPa. This high yield strength was attributed to a combination of solid solution strengthening ( $\sim 24\%$ ), grain boundary strengthening ( $\sim 14\%$ ), and hetero-deformation induced (HDI) strengthening ( $\sim 32\%$ ). The presence of coarse/fine grain interfaces, achievable through PBF-LB processing, was identified as a key factor contributing to HDI strengthening.

Hardness values for as-built WE43 have also been reported to be comparable to those of conventionally manufactured WE43. Upadhyaya et al. [113] measured a hardness of 79.4 HV0.2 for as-built WE43, although the orientation (build plane or transverse plane) was not specified. Differences in hardness between these planes have been observed [114], which are expected due to directional solidification leading to columnar grain structures and strong texture in PBF-LB WE43, as discussed in section 3.3.1.

Koch et al. showed that WE43 produced by PBF-LB outperforms cast alloy under cyclic compression at elevated temperatures [115]. This high temperature stability was attributed to the fine-grained microstructure and RE-precipitates. The well dispersed precipitates played an important role in enhancing creep resistance by impeding dislocation motion and stabilizing grain boundaries.

Overall, these studies demonstrate that the mechanical performance of PBF-LB WE43 is intimately tied to its unique process-dependent microstructure, comprising grain size, morphology, and RE-precipitate distribution. While the fine grains and dispersed precipitates contribute to enhanced strength and creep resistance, uncertainties remain regarding the influence of the thermal-history-driven microstructure on deformation behaviour. This needs further investigation, especially for load-bearing applications.

### 3.3.4 Degradation behaviour of PBF-LB WE43

As previously mentioned, certain RE-intermetallics are found in a large quantity in PBF-LB WE43. This has been shown to excessively accelerate the degradation in some typical corrosive environments due to the galvanic effects. The high corrosion rate of biodegradable Mg alloys desired for implants is a significant limitation. This is particularly due to the potential release of harmful hydrogen gas (according to the corrosion reaction of Mg presented in section 3.1.1) and the reduced mechanical integrity of the implant during critical

stages of bone healing. WE43 produced by AM has been found to corrode excessively (2-7.2 mm/yr) compared to cast WE43 (0.8-1.2 mm/yr) [101], [116]. Furthermore, Nilsson-Åhman et al. reported that hot isostatic pressing (HIP) of WE43 produced by PBF-LB may perform even worse because of growth of secondary intermetallic phases, leading to increased micro galvanic corrosion, as well as grain coarsening [102]. Efforts to improve the corrosion resistance of PBF-LB WE43 have included surface modification techniques such as protective coatings and pulsed laser surface texturing, both of which have shown potential for mitigating the degradation rate [117], [118]. However, it is important to accurately characterize the degradation behaviour of the bulk material as a first step.

### 3.3.5 Biological response to PBF-LB WE43

The knowledge on how WE43 produced by PBF-LB behaves in physiological conditions is still underexplored. Especially, the number of *in vivo* studies is limited, with the first being published as late as 2022 [119]. In said study, the degradation rate of the material was measured in comparison to *in vitro* results. An osteoconductive effect was confirmed *in vivo* by a higher amount of new bone having grown into the defect in place of the degraded scaffold, in comparison to the control. In terms of degradation time, the implant disintegrated *in vitro* after only 12 h, possibly due to the high surface area of the porous scaffolds. However, it remained intact for 4 weeks *in vivo*, showing no adverse effects on the area surrounding the implant. The large difference between the *in vitro* and *in vivo* degradation rate can be partly be due to the chosen implantation sites *in vivo*, as the amount of fluid in contact with the implant after implantation is reduced if the implant is mainly surrounded by fat and bone marrow. Additionally, the choice of degradation media used for *in vitro* testing can significantly influence the observed degradation rate, as it may not accurately replicate the physiological conditions present *in vivo* [120].

There are positive indications of *in vitro* studies of RE-containing Mg alloys produced by PBF-LB despite the high degradation rate. Xie et al. fabricated a porous 3D-printed Mg-Nd-Zn-Zr implant with suitable mechanical properties using PBF-LB which exhibited cytocompatibility in MC3T3-E1 and RAW267.4 cells and excellent osteoinductivity *in vitro* [121]. Li et al. also suggested that the corrosion resistance of porous WE43 scaffolds produced by PBF-LB could meet the requirements of biodegradable metal implants by means of Plasma Electrolytic Oxidation (PEO) surface treatments [122], further highlighting the potential of WE43 produced by PBF-LB as future implant material.

# 4 Experimental methods

In this thesis, PBF-LB was carried out for a WE43 Mg alloy. The influence of individual PBF-LB process parameters, including laser power, hatch distance and laser scan strategy, as well as build size and direction, on the resulting microstructure, mechanical properties, residual stress and texture was investigated. The methods applied are specified in this section, and a schematic overview is presented in Figure 4.1. Note that corrosion and biological response of the printed material are included in the manuscripts (I and II) but not in this thesis and are therefore not covered in the methods.

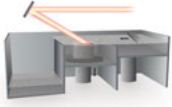





Powder bed fusion - laser beam	Macroscopic characterisation	Microscopic characterisation	Mechanical properties
	<ul style="list-style-type: none"> <li>• Defects               <ul style="list-style-type: none"> <li>◦ Porosity</li> </ul> </li> </ul>  	<ul style="list-style-type: none"> <li>• Microstructure               <ul style="list-style-type: none"> <li>◦ Texture</li> </ul> </li> <li>• Residual stress</li> </ul>  	<ul style="list-style-type: none"> <li>• Tensile</li> <li>• Compressive</li> <li>• Hardness</li> </ul> 

Figure 4.1. Overview of the methods applied in this thesis.

## 4.1 Powder bed fusion – Laser beam

All samples in this thesis were fabricated using PBF-LB on the same system to ensure consistency across builds. The EOS M100 (EOS GmbH, Germany) printer system used in the work was equipped with a continuous ytterbium fiber laser without any modifications. The powder used for the PBF-LB of samples was gas-atomized Mg alloy WE43 (Mg-4wt%Y-3wt%Nd-0.5wt%Zr) powder with particle size 23-60  $\mu\text{m}$ , supplied by NMD GmbH (Germany) using industrial grade feedstock materials. To minimize oxygen contamination, argon gas was utilized during the PBF-LB process, ensuring an oxygen content below 0.1%.

Samples were fabricated with a laser focus diameter of 40  $\mu\text{m}$  and a layer thickness of 20  $\mu\text{m}$  for each powder bed deposition and a scan speed of 1100 mm/s. In terms of laser power, hatch distance and laser scan strategy, the chosen values are presented for each individual study in Table 4.1. For Study III and Study IV, samples were also printed using two different build orientations

on the build plate, vertical (V) and horizontal (H). An overview of the laser scan rotations employed throughout the thesis is illustrated in Figure 4.2.

Table 4.1. Overview of process parameters used throughout the thesis. Note that for Study II, process parameter optimization was also included in the manuscript, the values given in this table are the final, chosen parameter sets. Build directions are given as vertical (V) and horizontal (H).

<i>Study #</i>	<i>P (W)</i>	<i>h (μm)</i>	<i>Scan strategy (° rotation)</i>	<i>Build-direction</i>
I	60, 80, 90	50	67	V
II	80, 90	40, 50, 60	67	V
III	80, 90	40, 50, 60	90, 67	V/H
IV	90	60	90, 67	V/H
V	90	60	0, 60, 120, 180, Chess	V

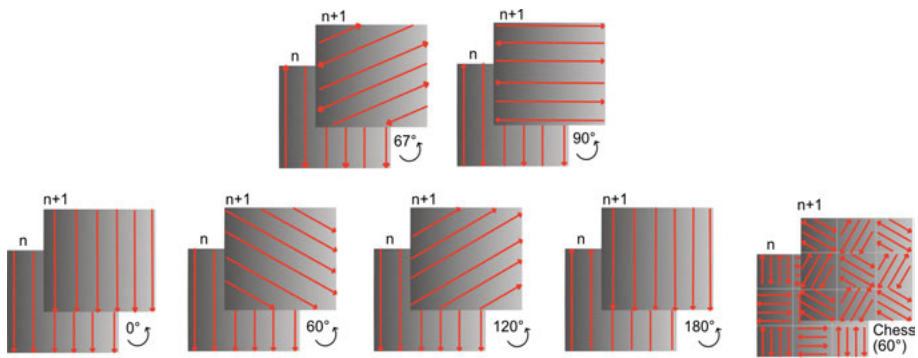


Figure 4.2. Schematic overview of the laser scan strategies employed throughout the thesis. The layer rotation between layer  $n$  and consecutively scanned layer  $n+1$  is illustrated.

## 4.2 Build quality

To ensure that the samples printed with the optimized process parameters were of sound quality, they were first visually inspected to assess the presence of cracking, distortion or over-melting. The relative density of the samples was subsequently measured by the buoyancy method, and internal defects such as lack-of-fusion porosity were observed using light optical microscopy (LOM). In addition, neutron tomography was used in Study V to further evaluate the porosity of printed samples.

**Relative density measurement** was performed to assess and assure satisfactory porosity levels for PBF-LB material, enabling effective comparison

between the quality of printed parameter sets to evaluate material performance. Before the density measurements, all samples were thoroughly cleaned in an ultrasonic bath consisting of ethanol. The weight of the sample ( $W_1$ ) was measured in air at room temperature (RT). The samples were then immersed in water or ethanol, and the weight ( $W_2$ ) was measured at RT. The relative density of the sample was calculated by Archimedes principle as follows:

$$\text{Relative density (\%)} = \left[ \frac{(W_1 \cdot \rho_1)}{(W_1 - W_2) \cdot \rho_2} \right] \cdot 100. \quad (\text{Eq. 4.1})$$

The density of ethanol at RT ( $\rho_1$ ) was taken to be  $0.789 \text{ g/cm}^3$ . The absolute density ( $\rho_2$ ) of conventionally cast WE43 ( $1.84 \text{ g/cm}^3$ ), measured using Archimedes' principle, was used as the reference. The weight of the samples was measured using a high-precision ( $\pm 0.1 \text{ mg}$ ) electronic balance (Mettler Toledo ML104).

**Light optical microscopy** is a fundamental technique for surface analysis in materials science. In this work, LOM was used mostly to evaluate internal defects such as pores and cracks. The samples were prepared for LOM by first mounting cut and cleaned parts in Bakelite. The mounted sample was then subsequently ground using silica papers and polished using oxidized porous silica (OP-S; Struers, Copenhagen, Denmark). The samples were afterwards etched in 2% Nital (2%  $\text{HNO}_3$  in Ethanol) for 5 s, allowing further evaluation of the melt pool morphology. The microscope used was an Olympus AX70 Research Microscope (Evident, Japan).

**Neutron** tomography is a non-destructive imaging technique that relies on the attenuation of a collimated neutron beam as it passes through matter. The variations in attenuation, caused by differences in material composition and thickness, are used to reconstruct a three-dimensional image of the sample's internal structure. In materials science it is valuable e.g. for quantifying porosity and pore connectivity. In Study IV in this thesis, neutron tomography was used to characterize the size and distribution of pores throughout the sample volume. The measurements were performed at the DINGO beamline (OPAL-reactor, Australian Centre for Neutron Scattering, Sydney) [123], with the L/D ratio set to 500 (L = distance from the neutrons source pinhole to the sample, D = pinhole diameter). An AWO ASI2600MM Pro CMOS camera ( $6248 \times 4176$  pixels) was used in combination with a Carl Zeiss 100 mm fixed-focal-length lens, providing an effective pixel size of  $15.7 \text{ }\mu\text{m}$ . Exposure time

was set to 120 s per projection with a total number of 1895 projections, separated by an angular step of 0.19°.

### 4.3 Microstructure characterization

This section describes the methods used to characterise the microstructure of the fabricated Mg samples throughout the thesis. Scanning electron microscopy (SEM) was employed to examine grain structure and phases, while Energy-dispersive X-ray spectroscopy (EDS) was used for elemental analysis. Phase identification and crystallographic information were obtained using X-ray diffraction (XRD).

**Scanning electron microscopy** is a powerful tool in metallography, allowing detailed analysis of e.g. surface topography and grain structure. In this thesis, backscatter electron (BSE) imaging was used. BSEs are high-energy electrons from the primary beam that are scattered back out of the sample after interacting with its atoms. The probability for this increases with increasing atomic number [124]. This means that heavier elements (as Y, Nd and Zr) backscatter more electrons and thus appear brighter, whilst lighter elements (as Mg) backscatter fewer electrons and appear darker. As the secondary phases in WE43 mainly consist in REE-rich intermetallics, their size and distribution are clearly visible using BSE. The same sample preparation was used for SEM as for LOM, however the samples were not etched for SEM. Images were in general taken at an accelerating voltage of 10-15 kV with a Zeiss 1530 or 1550 SEM.

**Energy-dispersive X-ray spectroscopy** is an analytical technique often used together with SEM analysis, that allows the determination of elemental composition of a material. When the electron beam strikes the sample, it emits characteristic X-rays unique to each element, allowing for qualitative and quantitative analysis of the elements present in the scanned area. In this work, an EDS detector (Oxford Instruments, Oxford, UK) was used in Study IV to identify the secondary phases. An acceleration voltage of 10 kV and a beam current of 1.8 nA was applied.

**X-ray diffraction** is one of the most commonly used techniques in materials characterisation, especially for crystalline solids. Since each crystalline phase generates a distinct diffraction pattern, XRD is commonly employed to identify unknown crystalline phases by comparing them to reference patterns. It is also used to estimate the relative quantities of different phases in multiphase

materials. The in-house XRD experiments conducted for this thesis (Study III, IV and V) were performed using a Siemens D5000 Diffractometer with Cu  $K\alpha$  radiation (wavelength 1.5406 Å) and a Bragg Brentano arrangement. The obtained diffractograms were analyzed using Rietveld refinement [125] to estimate the phase composition using Fullprof software [126]. Synchrotron radiation can also be used to produce X-rays by accelerating electrons in a large storage ring. A description of synchrotron experiments included in the thesis can be found under section 4.4.

## 4.4 Residual stress analysis

This section describes the methods used to measure residual stresses in the WE43 samples produced by PBF-LB. High-energy synchrotron X-ray diffraction (SXR) was employed to obtain high-resolution, non-destructive measurements of internal stresses.

**Synchrotron diffraction** is one of the most advanced techniques for non-destructive characterisation of local residual stress in materials, allowing precise mapping of internal stresses at the microscale. In Study III, the local residual stress was characterized in large WE43 samples using high energy synchrotron diffraction at the P61A Engineering Materials Science beamline (Helmholtz-Zentrum Geesthacht DESY, Hamburg, Germany). The transmission geometry setup and a beam spot size of 0.1x0.1 mm was used. The strain in two principal directions (longitudinal strain along the build direction and transversal strain in the build plane) were measured at each site in the samples, with six sites measured in total for each sample. The sample geometry and the measurement sites are presented in Figure 4.3.



Figure 4.3. The six measurement sites for synchrotron diffraction. The build direction is in the longitudinal direction.

The stress measurements were done using the  $\sin^2\psi$  method, and Pawley peak fitting was employed for fitting the obtained diffraction patterns. TOPAS-Academic [127] was utilized to analyse the diffraction data. The basic crystal structure information required for the Pawley refinement was obtained from

the Inorganic Crystal Structure Database (ICSD) [128]. The full diffractogram was subjected to Pawley refinement, where peak profiles were modelled with a modified Thompson-Cox-Hastings pseudo-Voigt (pV-TCHZ) profile function [127]. The background was fitted with a Chebyshev function consisting of six coefficients, and the zero-shift error together with instrument function was calibrated using a standard lanthanum hexaboride ( $\text{LaB}_6$ ) reference specimen. During batch refinement, instrument-related parameters were held constant, with only unit cell parameters and background being refined.

## 4.5 Texture analysis

This section details the techniques used to analyse the crystallographic texture of the WE43 samples. Electron backscatter diffraction (EBSD) was conducted to assess the local texture, i.e. the preferred orientation of grains, while neutron diffraction was used to evaluate the bulk texture of the material.

**Electron backscatter diffraction** is a technique used to analyse the crystallographic structure of materials. It provides information on grain orientation by detecting patterns formed when backscattered electrons diffract from the crystal lattice of a tilted sample surface. These orientations are projected stereographically onto a reference crystal axis. The data can be presented as color maps that visualize crystal orientations by assigning a color to each unique orientation. A common method is the inverse pole figure (IPF) coloring scheme, where crystallographic directions are mapped to RGB colors. This relies on a color key that links crystallographic directions to the specific colors. In Study IV and V, a Zeiss Merlin SEM (Germany) was used. The acceleration voltage was 20 kV and the beam current was set to 15 nA. A step size of 0.7  $\mu\text{m}$  was used, and grain boundaries were defined as having a misorientation greater than 15°. The data were analysed using Aztec Crystal 6.0 software from Oxford Instruments (Abingdon, UK).

**Neutron diffraction** can be used to study preferred orientation in polycrystalline materials. Neutrons are ideally suited to investigate bulk texture of specimens, as they have superior penetration in many materials in comparison to electrons or X-rays. This is because neutrons are scattered primarily by the atomic nuclei and not by the electrons, as is the case for X-rays. To determine the bulk texture of the as-printed components, neutron diffraction was used to measure a large sample volume of 10 mm diameter cylinders in Study IV and V. This ensures that observations are representative of the whole sample.

In study IV, measurements were performed on the MEREDIT instrument at the Nuclear Physics Institute, Czech Republic. Samples were fixed on the Euler goniometer and rotated along  $\varphi$  (0–360°) and  $\chi$  (0–90°) angles with a step of 5°. Variation of neutron diffracted intensities for 6 individual reflections [(100), (002), (101), (102), (110) and (103)] were collected for each orientation, using a neutron wavelength of 1.46 Å.

In Study V, measurements were performed on the KOWARI instrument at the OPAL-reactor (Australian Centre for Neutron Scattering, Australia) using a neutron wavelength of 1.75 Å. Measurements were at four detector positions (40°, 71°, 82° and 100°) in order to collect pole figure intensities for 7 individual reflections [(100), (002), (101), (110), (103), (112), and (201)]

In both Study IV and V, the orientation distribution function (ODF) was calculated for each sample, and pole figures for predefined reflections were calculated for easy comparison of all samples. Pole figures are maps of selected crystallographic planes plotted with respect to the sample frame, where each point on the pole figure represents the direction of a specific crystallographic plane as seen from the sample's perspective.

## 4.6 Evaluation of mechanical properties

This section outlines the methods used to evaluate the mechanical properties of the Mg alloy samples. Tensile and compression testing were performed to determine strength and deformation behaviour under uniaxial loading, while hardness testing was conducted to assess the material's resistance to localized plastic deformation.

**Tensile testing** provides key properties such as ultimate tensile strength, yield strength, elongation, and Young's modulus, helping to assess the materials strength and ductility. It is commonly employed as a standard material testing method and is a valuable test to allow comparison to other studies. As-built tensile specimens (diameter 1.4 mm) were tested directly in Study I and II, whilst in Study IV, dog-bone samples (4C20, diameter 4 mm) were machined from printed cylinders with a diameter of 10 mm. This was to make sure that the tensile behaviour accurately represents the bulk material response without the influence of surface regions. The influence of laser power, hatch distance, build orientation and laser scan strategy on the mechanical response of the as-built material was evaluated by tensile tests performed at room temperature for Study I, II and IV respectively. Each tensile test was performed using a displacement rate of 1 mm/min (strain rate  $1.67 \times 10^{-3} \text{ s}^{-1}$  for the smaller samples and  $5.56 \times 10^{-4} \text{ s}^{-1}$  for the larger samples) [129]. In Study I and IV, the

fracture surfaces of samples tested were evaluated using SEM as described in section 4.3.

**Compression testing** is a necessary method for testing implant materials, especially those intended for bone replacement, as bone largely undergoes compressive load *in vivo* and has a higher compressive than tensile strength [130], [131]. Compression testing provides key properties such as compressive strength and yield strength, which aids in assessing an implant material's ability to withstand physiological loading and maintain structural integrity in the body. Compression testing was performed using a Shimadzu AGS-X universal testing machine (Shimadzu, Kyoto, Japan) equipped with a 5 kN load cell. Cylindrical samples with a height-to-diameter ratio of 2:1 (diameter 3.5 mm, height 7 mm) were tested at room temperature under displacement control. A load rate of 1 mm/min was applied. The tests were conducted along the build direction of the samples (i.e. load direction is in the build direction). Load and displacement data were recorded continuously, and engineering stress–strain curves were generated for analysis. Fracture surfaces of tested samples were evaluated using SEM as described in section 4.3.

**Hardness** testing is frequently performed in order to characterize the material's ability to resist plastic deformation. Microhardness testing was carried out using a Vickers microhardness tester (MMT-X, Matsuzawa Co. Ltd, Japan). A load of 980.3 mN was applied with a dwell time of 13 seconds. Measurements were performed on polished cross-sections of the samples. 20 indentations were made for each measurement to ensure statistical reliability. The diagonal lengths of the indentations were measured by the machine, and the Vickers hardness values were calculated accordingly. In Study III, the measurements were made in the bulk at the top, centre and bottom of the sample in the transverse plane to the build direction. In Study V, measurements were performed in the bulk and near-edge regions for the build plane as well as the transverse plane.

## 4.7 Statistical analysis

Statistical analysis was used to ensure that conclusions were drawn based on meaningful interpretations of data. GraphPad Prism (version 8.0.0 and 10.4.2 for Windows, GraphPad Software, San Diego, California, USA) were used to perform statistical analyses. For all tests, a normality test was carried out to assess normal distribution affecting the choice of parametric or non-parametric tests. Statistical significance was noted at  $p < 0.05$ .

## 5 Summary of key results

This section presents the key results obtained in Study I to V. The results are presented separately for each study.

### 5.1 Study I: Higher laser power improves strength but reduces corrosion resistance of Mg WE43 processed by powder bed fusion

The first study of this thesis investigated the influence of three sets of laser powers (60 W, 80 W, 90W) on microstructure and the resulting mechanical properties. Microstructural characterization clearly revealed two types of microstructural regions in the samples, cellular and dendritic, as seen in Figure 5.1. Higher laser powers produced a greater proportion of dendritic grain structures, especially near the edges of the samples. In contrast, the cellular regions were more noticeable for lower laser powers. Quantification of secondary phase content showed a significantly higher presence in dendritic regions (~24.6%) compared to cellular regions (~17.6%). Additionally, results from EBSD pole figures revealed that areas with smaller, equiaxed dendritic grains had weaker texture as compared to the larger grains that presented basal texture in the build plane.

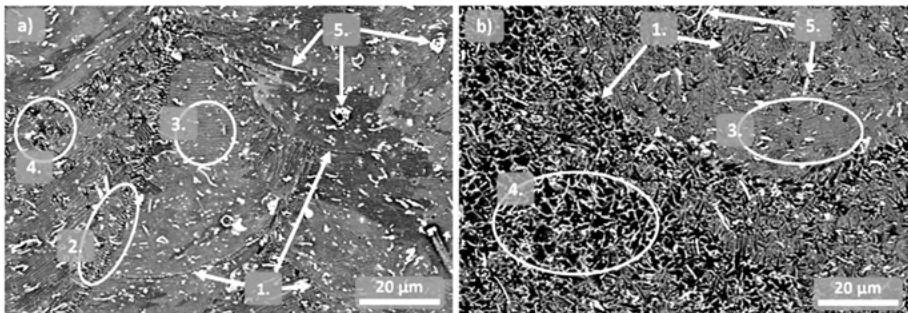


Figure 5.1. Representative images of the two types of microstructural regions observed in the samples, namely a) cellular and b) dendritic. The following are marked in the images: 1. the melt pool boundaries, 2. the cellular structure perpendicular to the melt pool boundary, 3. the cellular structure parallel to the melt pool boundary, 4. dendrites, and 5. oxides. Adapted from [132], licensed under CC BY 4.0.

For the cylindrical samples, printed with 5 mm diameter, the 60W, printed with the lowest energy input, showed a larger amount of lack-of-fusion porosity. However, these lack-of-fusion pores were not observed in the tensile test specimens, printed with a diameter of 1.4 mm. Instead, the higher laser power samples presented a higher degree of keyhole porosity.

Despite the higher degree of porosity in the higher laser power tensile samples, the mechanical properties were superior in the higher power samples as shown in Figure 5.2. Specifically, the 90 W samples exhibited the highest yield strength ( $\sigma_Y$ ), ultimate tensile strength ( $\sigma_{UTS}$ ), and elongation at failure ( $\epsilon_f$ ), while the 60 W samples demonstrated the lowest values across all parameters.

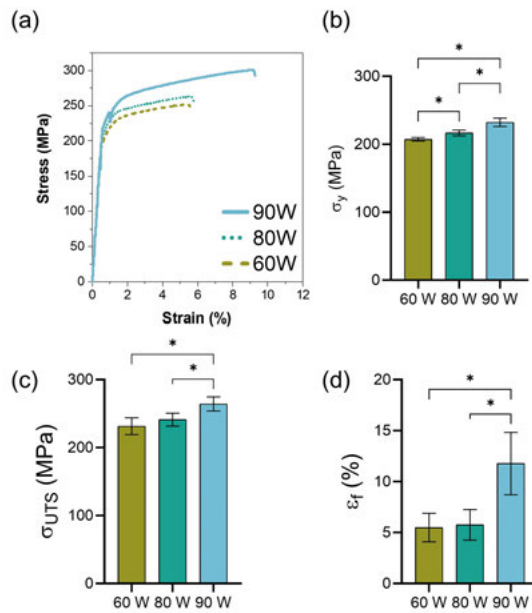


Figure 5.2. Results from the tensile tests (n=5 per group), showing a) representative stress-strain curves for the samples produced with the different laser powers, b) yield strength, c) ultimate tensile strength and d) elongation at failure. Statistically significant differences between groups are shown for  $p < 0.05$  (\*). Adapted from [132], licensed under CC BY 4.0.

Fractographic analysis (Fig. 5.3) supported these results, with the 60 W samples showing signs of brittle fracture, including localized cleavage planes, while the 90 W samples showed more ductile features along with visible porosity in the fracture planes.

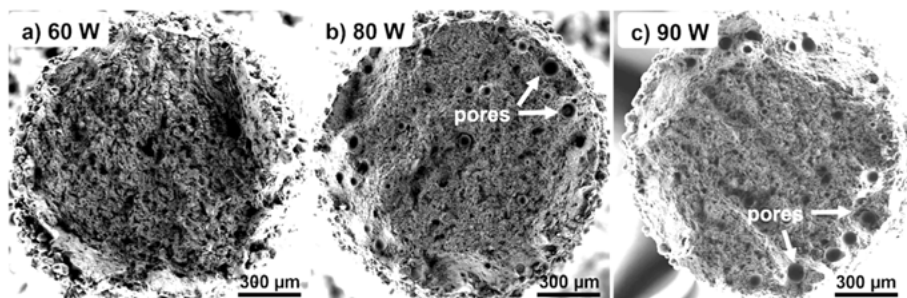


Figure 5.3. SEM images of the fracture surfaces for samples produced with (a) 60 W, (b) 80 W, and (c) 90 W. Adapted from [132], licensed under CC BY 4.0.

In summary, the increase in laser power led to improved mechanical strength and ductility, despite an increase in keyhole porosity for thinner samples. As a result, the samples produced with a laser power of 90 W exhibited the highest tensile properties and was kept as the ‘optimal’ laser power throughout the continuation of the thesis. However, all laser powers under study resulted in near-full density, and adequate mechanical properties. The study highlights the need of studying the material properties of the intended final geometry of PBF-LB components, as microstructure, porosity and final mechanical properties vary with sample size and shape.

## 5.2 Study II: Laser hatch distance can tune corrosion behavior and mechanical properties while maintaining *in vitro* biocompatibility of additively manufactured Mg alloy WE43

The importance of three sets of hatch distances (40  $\mu\text{m}$ , 50  $\mu\text{m}$  and 60  $\mu\text{m}$ ) in PBF-LB processing of Mg alloy WE43 was studied in the second project. The same two subgrain morphologies were identified as in Study I, namely dendritic and cellular. In terms of grain size, sample h60 (i.e. hatch distance 60  $\mu\text{m}$ ) exhibited a grain size distribution with the lowest number of smaller grains (Figure 5.4 a), followed by h50 and lastly h40. The EBSD orientation maps (presented for sample h60 in Figure 5.4 b) show that samples mainly exhibited a grain structure with large basal grains. The h60 samples exhibited the weakest texture, followed by h50 and lastly h40.

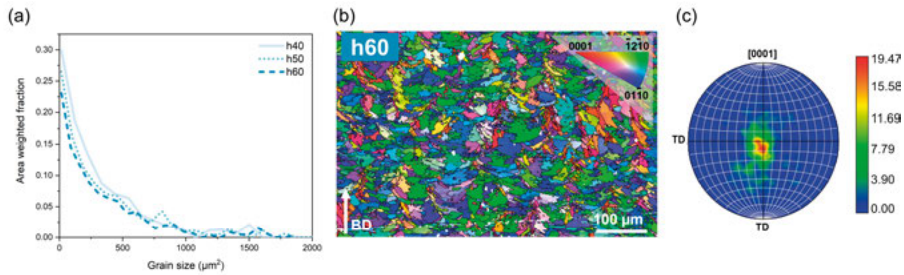


Figure 5.4. a) Grain size distribution as defined by grain area ( $\mu\text{m}^2$ ), b) EBSD orientation maps of samples produced with hatch distance  $60 \mu\text{m}$  and c) corresponding pole figure. The inverse pole figure (IPF) colour is set in the image plane. Adapted from [133].

The tensile test results showed that the h40 samples presented significantly higher  $\sigma_{\text{UTS}}$  and  $\sigma_{\text{Y}}$  than the h60, which presented the lowest (Figure 5.5). No statistical difference between the  $\sigma_{\text{Y}}$  of h40 and h50 could be established, nor between the  $\sigma_{\text{UTS}}$ . There was no statistically significant difference in terms of  $\epsilon_{\text{f}}$  found between the three sample groups in Study II.

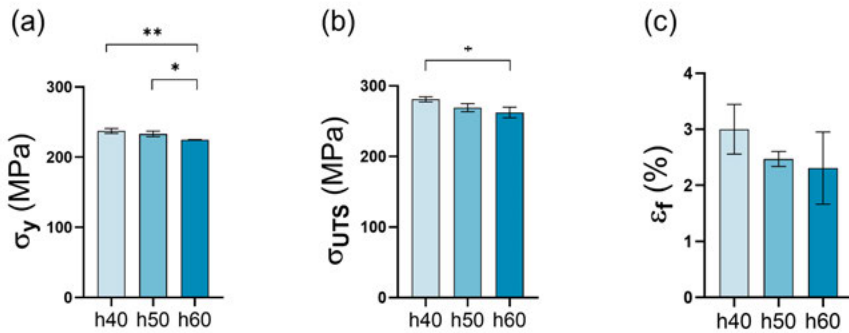


Figure 5.5. Average a) yield strength, b) ultimate tensile strength, c) elongation at failure. Error bars indicate standard deviations. Statistically significant differences are showed according to p value:  $p < 0.05$  (\*),  $p < 0.01$  (\*\*). Adapted from [133], licensed under CC BY 4.0.

Worth to note is that the  $50 \mu\text{m}$  sample in this study has the same process parameters as the 90 W sample in Study I. In terms of  $\sigma_{\text{UTS}}$  and  $\sigma_{\text{Y}}$ , no statistical difference between sample 90W and sample h50 (i.e. printed with the same parameters and sample geometry at separate times) was found. The elongation was, however, lower for the h50 sample than for the 90W sample from Study I ( $2.5 \pm 0.1$  vs  $10 \pm 2$ ).

Lastly, the h40 sample was produced with a laser power of 80 W, as opposed to the 90 W established for the h50 and h60 samples through process

parameter optimization (optimizing for dimensional stability and total porosity). Even so, it exhibited the highest tensile strength. This is in contradiction to previous observations made in Study I, where a decrease in laser power from 90 W to 80 W led to a significantly lower tensile strength. This highlights the possibility of using hatch distance as a tool to maintain tensile strength, when a lower laser power is applied.

### 5.3 Study III: On the relationship between process parameters and residual stress in large WE43 builds produced by PBF-LB

The third study of the thesis highlighted the effect of PBF-LB process parameters on residual stresses formed in a Mg WE43 alloy, specifically in large builds. From visual inspection, all printed samples regardless of size, exhibited consistent geometrical integrity with no visible distortion. However, a crack was observed in a large vertically printed cuboid during removal from the build plate, indicating high levels of residual stress which could lead to possible scale-up issues.

SEM analysis revealed microstructural features typical of PBF-LB processed WE43 alloys, including clear melt pool boundaries and areas of dendritic grains, primarily at the top and edges of the samples, but also present in the bulk of the material. No large zones of porosity were observed in the microstructure analysis. Comparative SEM imaging of edge vs. centre and top vs. bottom of large samples indicated similar variations in terms of morphology as in smaller printed samples as in Study I and II, suggesting limited influence of build size on microstructure. However, the measured Vickers microhardness was lower towards the top of the samples, as compared to in the centre of the bulk ( $88 \pm 3 \text{ HV}_{0.01}$  vs.  $95 \pm 4 \text{ HV}_{0.01}$ , respectively).

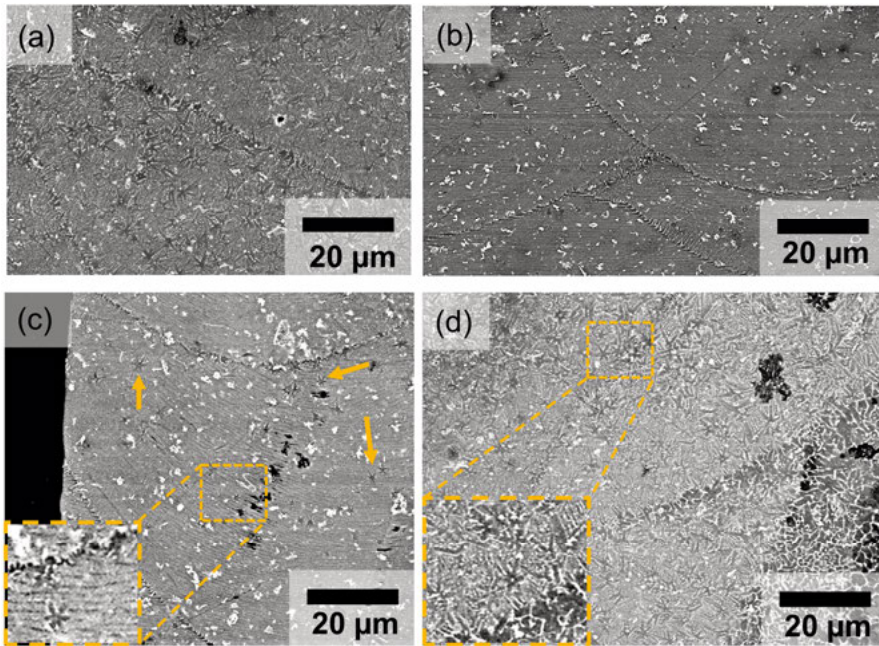


Figure 5.6. SEM images depicting the microstructure of the large sample printed with hatch distance 50  $\mu\text{m}$  and scan strategy 67°. (a) represents the centre of the top of the sample, (b) represents the bottom of the sample, (c) represents the centre of the bulk and (d) represents the edge of the sample. Yellow arrows in (c) show dendrites.

XRD measurements confirmed  $\alpha\text{-Mg}$  as the dominant phase across all sample regions (top, middle, bottom), with no significant variation in peak intensity or width. However, printed samples showed reduced intensity of the Mg (002) peak compared to the powder (when measured on the transverse plane to the build direction), indicating texture formation with c-axis alignment along the build direction. Synchrotron measurements confirmed  $\alpha\text{-Mg}$  as the main phase and enabled quantification of residual stresses. High tensile stresses were found at the edges of the samples, for all print conditions. Scan strategy significantly influenced stress profiles; a 90° rotation yielded consistent stress profiles across hatch distances. In contrast, the 67° rotation with 40  $\mu\text{m}$  hatch distance showed more compressive stress at the top, indicating altered thermal gradients. Build size and orientation also affected stress distribution, where larger vertical builds exhibited greater variation in stress across height for the longitudinal component.

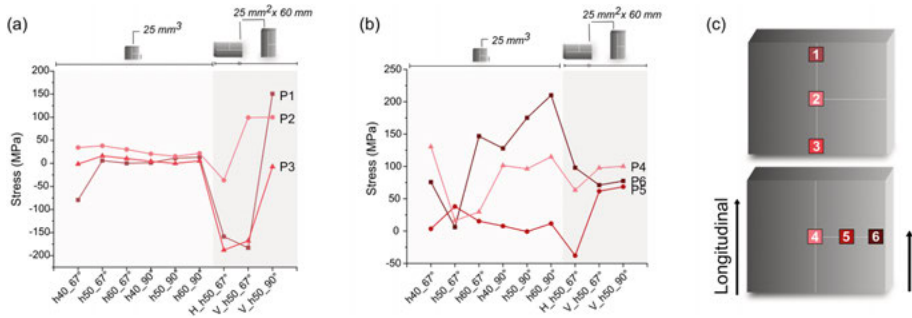


Figure 5.7. Residual stresses for the samples from synchrotron diffraction for all samples. (a) 1-3 and (b) 4-5, in the longitudinal direction. Insert of the points of the measurements are seen to the right of the figure.

## 5.4 Study IV: Leveraging laser powder bed fusion to alter texture and mechanical properties of magnesium alloy WE43

In Study IV, the influence of PBF-LB laser scan strategies ( $67^\circ$  and  $90^\circ$  rotation between consecutively scanned layers) and build directions (vertically printed on the build plate vs horizontally printed on the build plate) on the texture and mechanical properties of Mg alloy WE43 was studied.

The microstructure of the printed samples was similar to that found in Study I, II and III. This was expected, especially since the process parameters for the V67 sample in this study are the same as for the h60 sample in Study II and III.

The main crystalline phase in both the virgin powder and printed samples was HCP  $\alpha$ -Mg, as observed using lab-based XRD. This is in accordance with the observations from Study III. In the printed samples,  $Y_2O_3$  was detected ( $\sim 2\%$ ) and  $YMg_3$  was present in the powder and in small amounts in horizontally built samples. The XRD patterns further showed indications of preferred orientation of grains. This was most evident when comparing build directions. Vertically built samples exhibited higher intensity in the (002) Mg peak for the build plane, indicating a preferred orientation of the c-axis along the build direction, which agrees with the findings from Study III. To capture the overall texture more accurately, neutron diffraction was used to characterize the texture in the bulk. The pole figures further confirmed the previous observation of a strong basal texture in the build direction. In terms of scan strategy, samples built with a  $67^\circ$  rotation exhibited strong out-of-plane basal texture, while those with a  $90^\circ$  rotation also showed some in-plane texture ('in-plane' meaning the crystal rotation with respect to the image plane) due to the

alternating scan strategy, as indicated by the pattern observed for the (002) pole (Fig. 5.8).

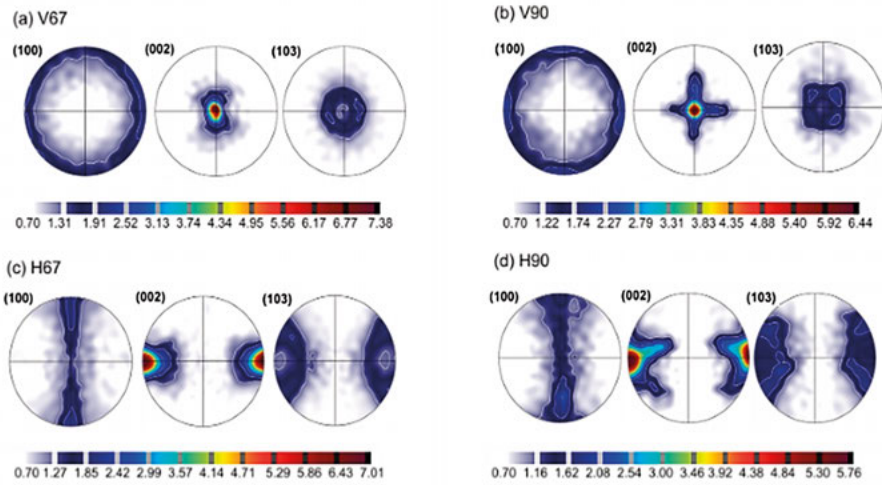


Figure 5.8. Calculated pole figures from neutron diffraction, showing preferential crystallographic grain orientations. Sample (a)-(b) are printed vertically and (c)-(d) are printed horizontally. 90 and 67 refers to the respective laser rotation between consecutively scanned layers. Adapted from [134] licensed under CC BY 4.0.

The mechanical behavior of the samples varied significantly with build orientation, clearly seen from the tensile test where the vertically built samples were loaded in the build direction whilst the horizontally built samples were loaded perpendicular to the build direction. Stress-strain testing demonstrated that samples printed horizontally achieved substantially higher yield strengths compared to vertically built ones. For instance, yield strength increased from  $143 \pm 8$  MPa to  $216 \pm 6$  MPa when moving from V67 to H67, and from  $130 \pm 10$  MPa to  $226 \pm 3$  MPa between V90 and H90. Statistical analysis confirmed that build direction had a significant effect on yield strength, while the influence of scan strategy was negligible.

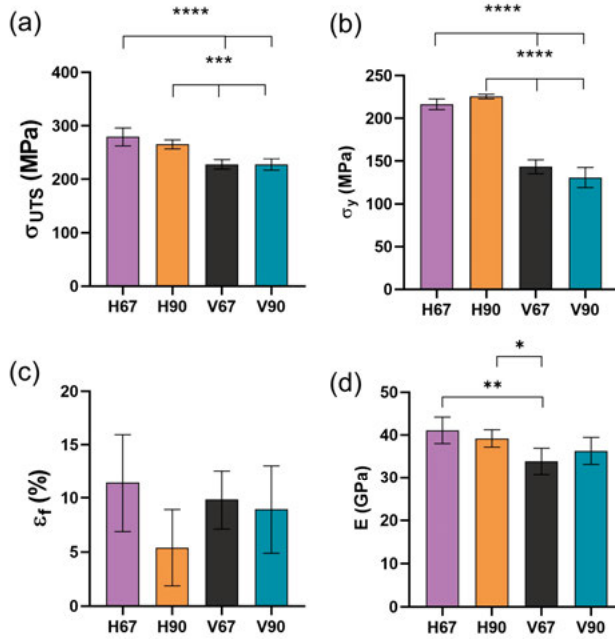


Figure 5.9. a) Yield stress, (b) Young's modulus (E), (c) Ultimate tensile stress, (d) elongation at failure (n = 5). Significance is showed according to p value:  $p < 0.05$  (\*),  $p < 0.01$  (\*\*),  $p < 0.001$  (\*\*\*),  $p < 0.0001$  (\*\*\*\*). Adapted from [134] licensed under CC BY 4.0.

Comparison between sample groups h60 from study II and V67 revealed notable differences in mechanical performance, despite being fabricated using identical process parameters. The differences between the samples are in regard to sample size and thus the influence of surface microstructure on the overall mechanical performance. The h60 samples, with a 1.4 mm diameter, would be susceptible to effects from the surface, or near-edge microstructure. The V67 samples on the other hand, with a diameter of 4 mm, more accurately represent the bulk material behavior. h60 samples exhibited significantly higher yield strength and ultimate tensile strength compared to V67. In contrast, V67 samples demonstrated higher elongation to failure.

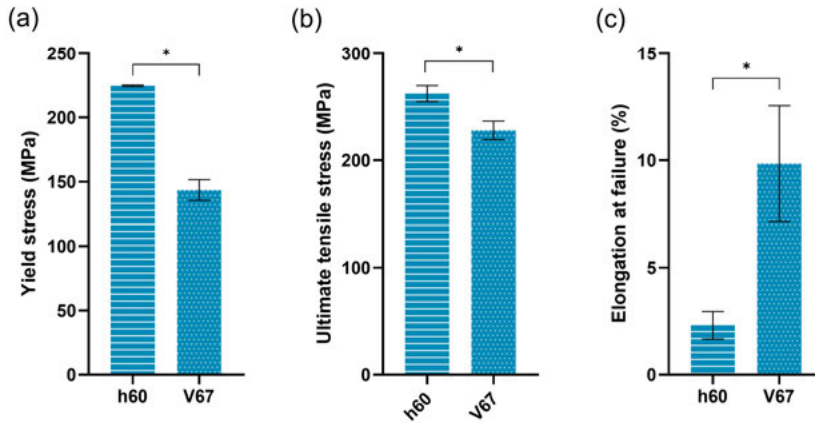


Figure 5.10. Comparison between h60 and V67, where a) Yield stress, b) Ultimate tensile stress, (d) elongation at failure. In all cases statistical significance ( $p < 0.05$ ) was found between h60 and V67.

In summary, while the scan strategy mainly impacted the in-plane texture of the printed WE43 samples, the build direction strongly influenced both the texture and mechanical properties. Horizontal builds demonstrated superior mechanical strength and stiffness. This suggests that keeping build orientation in mind during the design of the component is crucial for optimizing the performance of PBF-LB processed Mg alloys.

## 5.5 Study V: The role of laser scan rotation in additive manufacturing of Mg-RE alloy WE43

Study V provided further insight on the role of laser rotation on texture and resulting mechanical properties in PBF-LB of Mg alloy WE43. Five laser scan strategies were investigated, them being  $0^\circ$ ,  $60^\circ$ ,  $120^\circ$ ,  $180^\circ$  rotation between consecutively scanned layers, along with a chessboard strategy (called ‘Chess’ hereinafter).

The relative porosity measurements revealed that samples printed with  $0^\circ$  and  $180^\circ$  scan rotations exhibited significantly higher porosities (6.4% and 4.5%, respectively), while all other scan strategies resulted in porosities below 0.2%, indicating sufficient densification. Neutron tomography confirmed these findings, with pore volume fractions below 0.2% for the  $60^\circ$ ,  $120^\circ$ , and Chess samples. Pore distribution analysis showed random pore placement across the height for the  $60^\circ$  and  $120^\circ$  samples, while the  $0^\circ$ ,  $180^\circ$ , and Chess samples exhibited higher porosity near the baseplate. The Chess sample,

although considered fully dense, contained a few larger pores at the bottom, contributing to this effect.

SEM imaging showed large dendritic structures near the sample edges and finer equiaxed dendrites in the bulk, especially for the Chess sample. The 0° sample also showed dendritic areas adjacent to pores. Secondary phases were similar in distribution across all sample groups as confirmed by XRD analysis (~2% Y<sub>2</sub>O<sub>3</sub>).

Neutron diffraction analysis of bulk texture revealed strong out-of-plane basal texture in the 60° sample, comparable to previous studies. The 120° sample showed the highest texture intensity, particularly for the (002) and (101) poles, with a 3- and 6-fold texture symmetry in-plane. Despite the same internal rotation for the 60° sample and Chess sample, the intensity of the (002) pole is noticeable lower for the Chess sample indicating a weaker texture for when breaking the scan down into segments instead of scanning over the entire surface. The 0° and 180° samples showed the weakest texture, confirming that laser scan rotation significantly influences crystallographic orientation in PBF-LB processed WE43.

Compression testing showed brittle behaviour for all samples, and that the 0° sample had the lowest compressive strength and yield strength, with high variability in elongation to failure due to its high porosity, as can be seen also on the fracture surface (Fig. 5.11). The 180° sample performed better despite similar porosity levels, likely due to failure typically initiating at the top of the sample, whereas the porosity increased towards the bottom of the sample. The Chess sample demonstrated the highest compressive and yield strength, although no statistically significant differences were found between the Chess, 60°, and 120° samples.

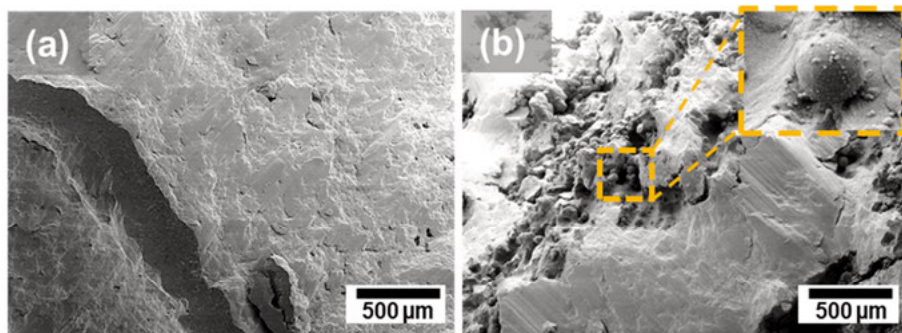


Figure 5.11. Fractography of sample (a) Chess and (b) 0°, with insert of porosity in the fracture surface.

Vickers microhardness testing (Figure 5.12) revealed a higher hardness in the plane transverse to the build direction (i.e. tested on the build plane) than in

the plane parallel to the build direction. The 0° and 60° sample showed the highest hardness in the bulk in the plane parallel to the build direction, indicating a material with adequate mechanical response when disregarding its high porosity. The 120° sample had the lowest hardness values overall in this plane. In the build plane however, a trend of the 60° and 120° sample presenting the highest hardness was found. Additionally, a significant difference in terms of the hardness in the bulk versus the near-edge microstructure was identified for sample groups 60 and Chess, in both tested planes. Overall, the values are in line with what was found in Study III. Overall, the findings from Study V highlight that laser scan rotation significantly influences porosity, texture, and mechanical performance in PBF-LB processed WE43.

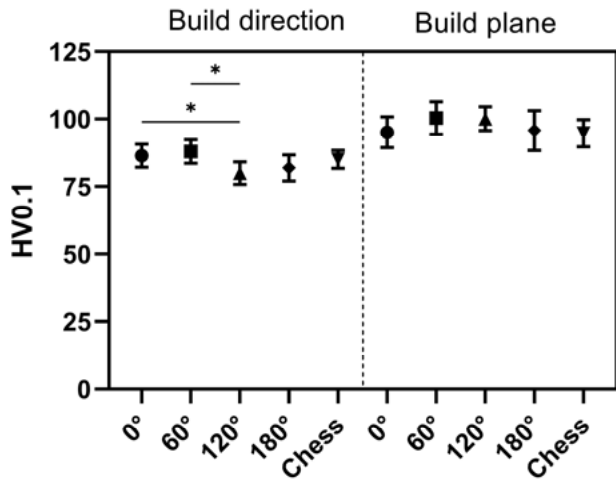


Figure 5.12. Microhardness values of the build direction and build plane in the bulk.

## 6 Thesis discussion

This thesis investigated the impact of variations in key process parameters in PBF-LB of Mg alloy WE43, specifically laser power, hatch distance, build size and orientation, as well as laser scan strategy. Across five experimental studies (Studies I–V), the connection between the abovementioned process parameters and the resulting microstructure, along with the effect on the residual stress, texture and mechanical performance of the printed material was demonstrated.

The first study established that a higher laser power leads to an increased formation of equiaxed-dendritic grains in WE43. This likely occurred because the warmer processing conditions associated with higher laser power leading to shallow local thermal gradients capable of promoting dendritic growth [104]. In contrast, the cooler processing conditions associated with lower laser powers favoured the conditions for cellular grains with having reduced secondary phases in the surrounding regions. Since the processing window of magnesium is relatively narrow, a certain degree of evaporation is expected with increased laser power [135], leaving behind more secondary phases in certain regions. Despite variations in grain morphology, all samples achieved mechanical properties within the range of what is previously reported for WE43 produced by PBF-LB (Table 6.1), while exceeding what has been reported for as-cast WE43. This suggests that even lower laser powers can produce mechanically sound parts, although with reduced strength.

Table 6.1. Values for tensile properties from Study I, II and IV, compared to values of WE43 from literature [94], [136]–[138].

Alloy	Yield strength (MPa)	Ultimate tensile strength (MPa)	Elongation to failure (%)
WE43 <sub>as-cast</sub>	133-150	179-206	4-6
WE43 <sub>extruded</sub>	221-304	295-352	11-22
WE43 <sub>PBF-LB</sub>	210-276	261-309	3-12
Study I	207-232	231-264	5-12
Study II	224-237	262-281	2-3
Study IV	130-226	228-279	6-12

While Study I demonstrated that increasing the energy input through laser power has the potential of enhancing the strength, Study II showed that modifying the melt pool overlap in terms of hatch distance is more limited in terms of tuning the mechanical behaviour. It is indeed an interesting point that even with fewer small grains ( $<100\ \mu\text{m}$ ) and a more isotropic grain orientation at larger hatch distances, tensile properties were preserved. The superior tensile properties of the h40 group relative to the h60 group can likely be attributed to differences in grain size distribution, as smaller grains tend to strengthen the material through the Hall-Petch relationship. It is noteworthy that, for the h40 sample the laser power applied was 80 W, as compared to 90 W for the h60 sample, meaning that despite the lower laser power a higher tensile strength was achieved. This is in contradiction to the previous observations made in Study I, where a decrease in laser power from 90 W to 80 W for a hatch distance of  $50\ \mu\text{m}$  led to a significantly lower tensile strength. This is likely due to the overall similar energy input, as a decrease in laser power would be counteracted by the smaller hatch distance (i.e. larger scan track overlap).

Sample 90 W from Study I and sample h50 from Study II were printed using the same parameters, yet presented statistically different elongation to failure. This may be due to the h50 samples being printed at a later time point, when powder had been re-used more times. A recent study on the powder re-use for PBF-LB of WE43 showed that there is a slight decrease in Mg content in re-used powder together with an increase in  $\text{Y}_2\text{O}_3$  and  $\text{RMg}_3$  phases [139]. The increase in oxides did not impact the mechanical properties investigated in terms of hardness, however, the impact on ductility was not investigated. In fact, the presence of  $\text{Y}_2\text{O}_3$  oxides in WE43 is known to cause stress concentrations and act as crack initiation sites in WE43 [140], thus a likely factor impacting ductility. The presence of  $\text{Y}_2\text{O}_3$  and  $\text{RMg}_3$  phases should further contribute to precipitation hardening by acting as obstacles to dislocation motion, increasing the yield strength and ultimate tensile strength of the alloy [141]. No statistical difference between sample group 90 W and h50 was found in terms of strength however, indicating that the extent of oxide formation, size or elemental variation due to powder re-use was insufficient to significantly alter the strengthening mechanisms.

In addition to the implications on mechanical performance, Study I and II also investigated the impact of the microstructure resulting from PBF-LB on the corrosion behaviour and biocompatibility of WE43. The higher energy input in Study I, and the subsequent formation of equiaxed dendrites, resulted in an increased amount of second phase precipitates thereby increasing the tendency for micro galvanic corrosion. Hence, despite the improved mechanical strength achieved

through higher laser power, the resulting microstructure is detrimental for the corrosion performance. In Study II, a more homogeneous distribution of Mg-RE precipitates, due to fewer and more homogeneously distributed grain boundaries of larger hatch distances, was found to decrease the corrosion rates. Importantly, the biocompatibility of the PBF-LB processed WE43 remained favourable (Study II), with osteoblasts showing good viability and proliferation, confirming its potential for biodegradable implant applications.

Whereas Studies I and II focused primarily on the implications of altering laser power and hatch distance on the microstructure and mechanical performance, Study III extended the investigation to the residual stresses. The third study introduced build size as a critical factor affecting the build quality, and clarified the resulting residual stress, hardness, and microstructure. Larger vertical builds exhibited greater stress variation across height as compared to the smaller, cuboid samples. However, the horizontally built samples showed a higher degree of residual stresses as compared to the cuboids, despite being printed to the same height. In fact, samples printed horizontally on the build plate would have generated long laser scan vectors along the length of the specimen for each alternating layer, as compared to the cuboid samples. Long scan vectors likely enhanced the thermal gradient along solidifying tracks trailing the passing laser, thereby increasing the tendency for solidification shrinkage. With increased shrinkage, the likelihood for build-up of residual stress was enhanced.

In terms of magnitude, the residual stress varied with processing parameters and in some cases approached the yield strength of WE43 (Table 6.1). The stress may locally exceed the yield strength, leading to stress relaxation through plastic deformation or fracture during part detachment. This phenomenon is well-documented in PBF-LB processes and can at times cause cracking. Although one crack was observed in the larger builds in Study III, no such defects appeared in the smaller samples printed for the rest of the studies. This relatively low susceptibility to cracking contrasts with alloys such as Inconel 718 [142], which are known to experience higher residual stress levels and a greater tendency toward cracking under PBF-LB conditions. WE43 thus demonstrates a higher tolerance to thermal stresses, improving its suitability for complex or large-scale builds.

Building on the confirmation that the highest degree of residual stresses was found for large, vertical builds, Study IV introduced build direction as a factor for evaluation of microstructure and mechanical properties. The strong basal texture aligned with the build direction observed is consistent with previous studies on WE43 [4], [103]. The higher yield stress for horizontally built samples, having the c-axis of grains perpendicular to the loading

direction, highlights the opportunity for using as-built microstructure to alter mechanical properties. Another reason, apart from the texture implications, for the higher mechanical response of the horizontally printed samples is likely the lower amount of residual stress, as observed in Study III.

In Table 6.1, all tensile properties from Study I, II and IV are presented and compared to values from literature. In general, the tensile values presented in this thesis are in the range of what is found in literature. The tensile behaviour differs significantly between small and large samples (Study I and II vs Study IV). This discrepancy can be attributed to differences in sample geometry and surface effects. For instance, thinner samples have shorter laser scan lengths and are more affected by the insulating effect of the surrounding powder. The thickness of the samples (1.4 mm) means that the surface regions, of mainly small, equiaxed grains, will have a larger influence on the overall performance, whereas the larger samples (diameter 4 mm) better represent bulk material behaviour, minimizing the influence of surface heterogeneities. In fact, the thinner tensile samples have a gauge thickness close to that of the strut size typically used in PBF-LB printed lattice structures [122], [143], implicating the importance of investigating the specific geometry for the intended application to avoid over- or underestimating the mechanical response.

One of the main findings of Study IV, was that the observed impact of scan strategy on texture. This contrasts previous studies, which have focused more on laser power and scan speed as key factors in shaping microstructure through their influence on melt pool dynamics and thermal gradients [5], [101], [103]. When changing the laser scan rotation, the orientation of the melt pools to one another along the build direction will change as the subsequent layer is being melted. The direction of heat extraction will vary between the two laser scan rotations, which leads to different orientations of grain growth in the melt pools the resulting differences observed for in-plane texture. However, the in-plane texture variations induced by scan strategy did not translate into statistically significant mechanical differences. For that reason, Study V investigated the role of laser scan rotation in achieving optimal densification and texture, with an emphasis on mechanical properties.

Comparing the 120° and 60° rotation samples (i.e. repeating the scan pattern every 3<sup>rd</sup> and 6<sup>th</sup> layer, respectively) shows similar texture development as the 67° (i.e. repeating the scan pattern every 360<sup>th</sup> layer, approaching perfect cylindrical, or ∞-fold, symmetry) from study IV. This may suggest that factors beyond heat distribution, such as scan path symmetry, or the layer-to-layer thermal history, could also influence texture evolution. Interestingly, the Chess sample, despite sharing the same internal rotation as the 60° sample, displayed less pronounced basal texture whilst maintaining high mechanical

properties. The microstructure of the Chess sample showed areas of dendritic grain growth both along the edge and also in the bulk of the material, to a higher extent than the other samples. This is a result of the overlap between the different segments, leading to an increased amount of re-melting in these regions leading to shallow local thermal gradients with increased likelihood of dendritic grain growth, which from Study I was found to lead to a higher mechanical performance in PBF-LB of WE43; likely a contributor to the mechanical performance of the Chess sample group despite its weaker texture.

For other alloys, a  $0^\circ$  rotation during PBF-LB has led to severe stress accumulation because the consistent scanning direction creates preferential thermal gradients and stress patterns that accumulate layer by layer, eventually causing macrocracks in the samples [144]. No such cracking was observed for the  $0^\circ$  and  $180^\circ$  samples; however, a lower level of densification was noted. The unidirectional path of the scan vectors is likely to promote the formation of shrinkage porosity along the edges of the melt tracks [145], facilitating pore formation. This effect could potentially have been mitigated by increasing the overlap between melt pools. Indeed, the process parameter optimization for the parameter set used throughout the thesis was based on rotational scan strategies, which likely resulted in insufficient overlap between adjacent scan tracks when applied to unidirectional scanning approaches.

From the microhardness results, a lower hardness was found in the near-edge region as compared to the bulk (trend seen for all sample groups, significant for  $60^\circ$  and  $120^\circ$ ). This is likely an effect of residual stresses at the edge, as tensile residual stresses at the edges are expected based on the results from Study III. When tensile residual stress is present, the material is more susceptible to plastic deformation, leading to lower hardness measurements [146]. This is likely also the reason for the lower hardness at the top edge of the large builds in Study III. Moreover, the hardness was higher in the build plane than on the transverse cross section, indicating anisotropy in the mechanical response. This is likely an effect of texture, as a strong basal texture is prevalent in the build direction, meaning that the alignment of the close packed crystallographic planes in this region offer increased resistance to indentation and plastic deformation.

This work has certain limitations, including limited generalizability beyond the WE43 alloy and the need for further optimization of process parameters, as results from the hatch distance study cannot be directly applied to subsequent studies (III, IV, V). However, the five studies presented in this thesis together provide an important step forward towards understanding how process parameters in PBF-LB are linked to the microstructure and mechanical properties. While each study highlights a specific set of process considerations, together, they are a clear demonstration that

all process parameters need to be considered as a whole, since it is the interaction between them all that determines the interplay between microstructure, residual stress and mechanical performance. This work advances the understanding of additive manufacturing of Mg alloys for reliable application in biomedical contexts in the future.

## 7 Conclusions

The work presented revolves around the aims and objectives formulated at the very beginning of the thesis (section 2). The following section provides more insight into the conclusions of the separate studies and how they are connected to the thesis as a whole.

In Study I, the importance of energy input, in terms of laser power, was established, for a set of otherwise optimized process parameters in terms of laser scan speed and hatch distance, for a set laser spot size and powder layer thickness. It was concluded that an increase in laser power from 60 W to 90 W resulted in an increase in the formation of smaller, equiaxed-dendritic grains, giving rise to a significantly higher tensile strength.

In Study II, a change in hatch distance, i.e. the overlap between scan lines, could be related to a change in size and texture of the larger grains in the microstructure. The tensile properties could thereby be maintained even for a larger hatch distance, giving fewer small grains and a more homogeneous grain size distribution of the basal grains. Hatch distance was hence demonstrated to be possible to use as a tool to maintain tensile strength, when a lower laser power is applied.

In Study III, build size had minimal influence on microstructure but significantly affected both hardness and the distribution of residual stresses within the samples. Larger vertical builds exhibited greater variation in stress across height, while laser scan strategy (67°- and 90°- rotation) had overall similar effects on the residual stress distribution within the alloy, with tensile residual stresses identified at the edges of the samples. These findings highlight a potential size limit for printable parts due to the detrimental effects of residual stress on mechanical integrity and degradation, particularly in biodegradable Mg implants.

In Study IV, both sample orientation and laser scan strategy were found to influence the in-plane and out-of-plane texture for PBF-LB of Mg alloy WE43. It was further showed that build direction has a pronounced effect on the tensile strength and Young's modulus of the material. However, while laser scan strategies of 67°- and 90°-rotation between layers influenced in-plane texture, this did not translate to a statistically significant effect on the mechanical properties.

In Study V, given the indications of a possible effect of the laser scan strategy, as well as the pronounced basal texture of additively manufactured WE43, the effect of laser rotation was further investigated, and found to have a significant impact on the densification, degree of texture and mechanical properties. Limited rotation between layers drastically reduced the densification, whilst a  $60^\circ$  or  $120^\circ$  rotation between layers resulted in a high degree of basal texture in the build direction. The segmented scan strategy was found to limit the texture whilst maintaining high mechanical properties.

All together, these studies demonstrate that the microstructure, texture, and mechanical behaviour of PBF-LB processed WE43 are highly sensitive to the interaction between laser energy input, scanning parameters, and build geometry. A careful balance of these parameters is therefore essential to achieve dense, low-stress, and mechanically reliable WE43 components, with tuneable biodegradation behaviour suitable for tailored lightweight structural applications.

## 8 Future perspectives

The main goal of this thesis was to deepen the understanding of the relationship between PBF-LB process parameters and the resulting microstructure, residual stress and mechanical properties of Mg alloy WE43. By highlighting the specific implication of each process condition, the work in this thesis highlights the necessity for continued research across a range of related topics.

Firstly, to implement a WE43 produced by PBF-LB in biomedical implants, its response to biological conditions when manufactured in thin-walled structures and complex geometries typical of implant designs needs to be investigated. The inherent anisotropy of WE43, which arises from the layer-wise nature of PBF-LB, may significantly influence its mechanical and biological performance *in vivo*. Understanding and controlling this anisotropy will be essential for ensuring consistent and reliable implant behavior. This weaves into the possible impact of powder re-use on the sample ductility. In terms of sustainability, optimizing powder usage and minimizing waste is crucial not only for cost-efficiency but also for reducing the environmental impact. Therefore, an understanding of how powder re-use affects both the mechanical response, as well as the biocompatibility of WE43, is essential for developing sustainable implants.

Secondly, further validation of WE43 as a biomaterial requires comprehensive studies on its *in vivo* corrosion behaviour and biocompatibility. The fatigue performance of WE43 under simulated physiological loading conditions must be thoroughly assessed. Since implants are subjected to cyclic stresses within the human body, understanding how the alloy responds to such conditions will be vital for predicting its lifespan and structural integrity.

Thirdly, the residual stresses introduced during the PBF-LB process can significantly affect the mechanical properties and dimensional stability of the final component. A focused investigation into the stress evolution while the part remains attached to the build plate could lead to valuable insights into the origins and distribution of these stresses. Such knowledge would inform strategies for stress mitigation, including optimized support structures, heat treatments, and build orientations, ultimately improving the reliability of PBF-LB manufactured implants.

Lastly, future research should also consider the broader implications of REE biocompatibility and investigate alloy systems beyond WE43. While REEs contribute to the desirable mechanical properties of WE43, their long-term biological effects remain debatable. Exploring alternative alloy systems that incorporate more biocompatible elements and are specifically developed for PBF-LB, could offer safer and more effective implant materials. One such candidate is the Mg-Ca-Zn alloy system, which not only consists of elements naturally present in the human body but also exhibits glass-forming capabilities. The amorphous structure achievable with these alloys translates into properties such as high toughness and significantly reduced corrosion rates because of their isotropic and homogenous nature. When combined with the design freedom and precision of PBF-LB, such alloy systems could represent a big step forward in the development of next-generation Mg-based implants.

## 9 Svensk sammanfattning

Laserbaserad pulverbäddsfusion (PBF-LB) av magnesiumlegeringen WE43 (Mg-4 vikt% Y-3 vikt% RE-Zr) har stor potential för utvecklingen av framtida biologiskt nedbrytbara metallimplantat. Denna avhandling undersöker hur centrala processparametrar inom PBF-LB påverkar mikrostruktur, restspänningar, textur och mekaniska egenskaper hos WE43. Syftet med denna kunskap är att stödja den fortsatta utvecklingen och den framtida implementeringen av PBF-LB-bearbetad WE43 för användning i biologiskt nedbrytbara, medicinska implantat. Effekterna av lasereffekt, skanningsavstånd (hatch distance), byggstorlek, byggriktning samt laserrotation har undersökts systematiskt.

En ökning av lasereffekten visade sig främja bildandet av dendritiska korn och förbättra draghållfastheten. Skanningsavståndet kunde användas för att bibehålla draghållfastheten även vid lägre lasereffekter, genom att påverka fördelningen av sekundära faser, kornstorlek och textur. En ökning av byggstorleken i den vertikala riktningen ökade även restspänningarna. Dragspänningar identifierades dessutom vid kanterna av proverna, vilket är vanligt vid PBF-LB-bearbetning. Detta korrelerade med en lägre hårdhet i materialet nära kanterna, jämfört med i bulkmaterialet. Byggriktningen hade dessutom en inverkan på både draghållfasthet och elasticitetsmodul, främst på grund av utvecklingen av en stark basal textur i byggplanet.

Vidare påvisades möjlighet till att skräddarsy textur med hjälp av laserrotation. Laserrotationer på 67° och 90° modifierade texturen utan att påverka de mekaniska egenskaperna, medan en begränsning av rotationen till 0° eller 180° kraftigt försämrade materialets densitet och som följd dess strukturella integritet. Laserrotationer på 60° och 120° belyste ytterligare möjligheten att skräddarsy textur medan en segmenterad skanningsstrategi erbjuder en balans mellan texturkontroll och mekanisk prestanda, tack vare ökad andel dendritiska korn och gynnsam porfördelning.

Sammantaget ger arbetet som ingår i denna avhandling en stabil grund för hur processparametrar kan optimeras för att uppnå önskvärda mikrostrukturella och mekaniska egenskaper hos WE43, vilket stödjer dess potentiella användning inom medicinska tillämpningar.

## 10 Acknowledgements

Throughout these years, I've learned countless valuable lessons, not only about science, but also about myself and life in general. I am incredibly proud to finally have this thesis in my hands and I would like to express my warmest gratitude to everyone who has supported me. This thesis is not only the result of my own efforts, but also a reflection of the generosity and encouragement I've received from so many.

To start, I want to thank my supervisors. *Cecilia*, thank you for all your unwavering support and thoughtful feedback throughout both my Master's thesis and PhD studies. I am thankful for all the time you have invested in me, and especially for helping me find the way forward scientifically when I was not able to. *Francesco*, thank you for the invaluable knowledge about magnesium! You have a real talent for turning science into something understandable, I feel lucky to have started in time to have you as a co-supervisor. *Tuerdi*, thank you for your patience, always insightful feedback, and expertise in synchrotron techniques. Your guidance has been invaluable and I regret not being able to dedicate more time to our collaborative work during the last year. *Per*, I want to thank you for always helping me when I reached out. And of course, thank you for the great support during the beamtime. I also want to thank *Martin S.*, although not a supervisor, you have helped shape the last two projects of my thesis, and for that I am very grateful. Your scientific input and the always super-quick feedback have been very helpful.

During my PhD, I had the privilege of collaborating with many talented and dedicated people whose contributions made a real difference in my work. *Vitalii*, I want to thank you for your fantastic work on the EBSD. I know it was not easy, and your patience was incredible. *Hanna*, thank you for paving the way for Mg in the group and always taking the time to help me, both when I first started as well as now when you are no longer working at the uni. It was great working with you. *Niccolò* and *Gry*, thank you for your great work on the biocompatibility testing; it has proved a valuable part of the manuscript. Thank you also to *Prabhat P.* for the help and input with the last neutron proposal. I want to thank *Vladimir* and *Florenca* at ANSTO. It was great to collaborate with you, and your efforts helped push the project forward in meaningful ways. Thanks also to *Premysl* and *Charles* for the support on the

neutron measurements at Řež, your expertise and assistance during the experiments were much appreciated.

To those who supported me behind the scenes! I want to thank *Carl-Johan* and *Jithin* for the support on the printers during my time as a PhD student, making tricky machines run smoothly. A big thank you also to *Pedro* for all the help with equipment in the chemistry lab. I am grateful to *Lars-Erik* and the guys in the workshop for all your great work on machining my samples throughout the years, I always knew I could count on you. Thank you to *Ingrid R.*, *Sara R.*, *Karin M.*, and *Gaia A.*, for your invaluable help with project coordination and administration. *Alexandra*, thank you for all the fun moments, the workplace has not been the same without you. I also want to thank *Stina W.*, and *Hanna O.*; your energy and support meant a lot to me.

A meaningful part of my PhD has been the experiences enabled by the *SwedNess* graduate school for neutron scattering. I would like to thank the Swedish Foundation for Strategic Research. A special mention here to *Camilla D.* for the organization of the great *SwedNess* events. Also, thank you to all the *SwedNess* students for the fun times during the trips. Especially to the Neutron Besties – I am so glad I have gotten to know you.

I also want to express how lucky I feel for having such amazing colleges at Uppsala University. A big thanks goes out to all current and previous members of the BMS group (*Alejandro*, *Charlotte*, *Susanne*, *Salim*, *Giulio*, *Yijun*, *Leon*, *Margarida*, *Laura*, *Zaki*, *Ioannis*, *Huasi*, *Belén*, *Himesh*, *Estelle*, *Morteza*, *Linglu*, *Francesca*, *Cole*, and *Stephanie*). I have had such wonderful moments and travels with you. A special mention goes out to the *DoA*, for always being such a supportive crew. *Ana*, thanks for being such a great office mate from day one. *Andrea*, you have been the best thesis-writing buddy one could ask for! *Estefanía*, thank you for always checking in on me and for your genuine kindness. The workplace would also not be the same without the amazing PhD students from Tribo and EMBLA (*Felix*, *Maria*, *Dimitra* and *Vidhiya* to name a few), you are so fun! I had the pleasure of working with some fantastic students during my PhD. Thank you to *Fanny Sandblad* and *Fanny Saarela*, it was great working with you. And thank you also to *Satya V.*, for all the 3D printing help (and of course for the donuts!).

To all the friends who have visited, travelled with me, or simply stood by my side – thank you for making these years special. I truly wouldn't be who I am today without each and every one of you. Jag vill också tacka dig, *Jonas*. Tack för att du alltid stöttar oavsett vilken del av livet det handlar om, du är min största trygghet. Stort tack även till din familj som tagit emot mig med så mycket värme.

Och till sist, en hel sida till dem som alltid stått vid min sida – min fina familj. Tack för all kärlek, tålamod och uppmuntran. Ett speciellt tack till *Kajsa* och *Gustaf*, mina fantastiska föräldrar, och Carl, min älskade bror. Även när jag är långt borta finns ni alltid nära i hjärtat. Tack för att ni alltid tror på mig.

# 11 References

- [1] Syntellix, “MAGNEZIX® – A MILESTONE IN MATERIAL RESEARCH.” <https://www.syntellix.de/en/products/technology.html> (accessed Dec. 01, 2024).
- [2] R. Tandon, T. Wilks, M. Gieseke, C. Noelke, S. Kaierle, and T. Palmer, “Additive manufacturing of electron® 43 alloy using laser powder bed and directed energy deposition,” in *Proceedings Euro PM 2015: International Power Metallurgy Congress and Exhibition*, 2015.
- [3] S. Gangireddy, B. Gwalani, K. Liu, E. J. Faierson, and R. S. Mishra, “Microstructure and mechanical behavior of an additive manufactured (AM) WE43-Mg alloy,” *Addit. Manuf.*, vol. 26, no. September 2018, pp. 53–64, 2018, doi: 10.1016/j.addma.2018.12.015.
- [4] H. Nilsson-Åhman, L. Thorsson, P. Mellin, G. Lindwall, and C. Persson, “An Enhanced Understanding of the Powder Bed Fusion – Laser and Experimental Characterization,” *Materials (Basel)*, 2022.
- [5] F. Bär *et al.*, “Laser additive manufacturing of biodegradable magnesium alloy WE43: A detailed microstructure analysis,” *Acta Biomater.*, 2019, doi: 10.1016/j.actbio.2019.05.056.
- [6] W. Jin and P. K. Chu, “Orthopedic Implants,” in *Encyclopedia of Biomedical Engineering*, R. Narayan, Ed. Oxford: Elsevier, 2019, pp. 425–439. doi: <https://doi.org/10.1016/B978-0-12-801238-3.10999-7>.
- [7] C. Lee, E. Mayer, N. Bernthal, J. Wenke, and R. V O’Toole, “Orthopaedic infections: what have we learned?,” *OTA Int. open access J. Orthop. trauma*, vol. 6, no. 2 Suppl, p. e250, May 2023, doi: 10.1097/OI9.0000000000000250.
- [8] World health organization (WHO), “Antimicrobial resistance.” <https://www.who.int/news-room/fact-sheets/detail/antimicrobial-resistance> (accessed Jun. 13, 2024).
- [9] A.-M. Wu *et al.*, “Global, regional, and national burden of bone fractures in 204 countries and territories, 1990–2019: a systematic analysis from the Global Burden of Disease Study 2019,” *Lancet Heal. Longev.*, vol. 2, no. 9, pp. e580–e592, 2021, doi: [https://doi.org/10.1016/S2666-7568\(21\)00172-0](https://doi.org/10.1016/S2666-7568(21)00172-0).
- [10] J. R. Jones, D. S. Brauer, L. Hupa, and D. C. Greenspan, “Bioglass and Bioactive Glasses and Their Impact on Healthcare,” *Int. J. Appl. Glas. Sci.*, vol. 7, no. 4, pp. 423 – 434, 2016, doi: 10.1111/ijag.12252.
- [11] S. K. Wong, Y. H. Wong, K.-Y. Chin, and S. Ima-Nirwana, “A Review on the Enhancement of Calcium Phosphate Cement with Biological Materials in Bone Defect Healing,” *Polymers (Basel)*, vol. 13, no. 18, 2021, doi: 10.3390/polym13183075.
- [12] J. Wang, J. Dou, Z. Wang, C. Hu, H. Yu, and C. Chen, “Research progress of biodegradable magnesium-based biomedical materials: A review,” *J. Alloys Compd.*, vol. 923, p. 166377, 2022, doi: <https://doi.org/10.1016/j.jallcom.2022.166377>.

- [13] K. Sangeetha, A. V Jisha Kumari, J. Venkatesan, A. Sukumaran, S. Aisverya, and P. N. Sudha, "13 - Degradable metallic biomaterials for cardiovascular applications," in *Fundamental Biomaterials: Metals*, P. Balakrishnan, S. M S, and S. Thomas, Eds. Woodhead Publishing, 2018, pp. 285–298. doi: <https://doi.org/10.1016/B978-0-08-102205-4.00013-1>.
- [14] A. R. Khan, N. S. Grewal, C. Zhou, K. Yuan, H.-J. Zhang, and Z. Jun, "Recent advances in biodegradable metals for implant applications: Exploring in vivo and in vitro responses," *Results Eng.*, vol. 20, p. 101526, 2023, doi: <https://doi.org/10.1016/j.rineng.2023.101526>.
- [15] G. Gaşior, J. Szczepański, and A. Radtke, "Biodegradable Iron-Based Materials—What Was Done and What More Can Be Done?," *Materials (Basel)*, vol. 14, no. 12, 2021, doi: 10.3390/ma14123381.
- [16] H. Yang *et al.*, "Alloying design of biodegradable zinc as promising bone implants for load-bearing applications," *Nat. Commun.*, vol. 11, no. 1, pp. 1–16, 2020, doi: 10.1038/s41467-019-14153-7.
- [17] Y. Zhang *et al.*, "Exploring the degradation behavior of biodegradable metals (Mg, Zn, and Fe) in human duodenal fluid," *J. Magnes. Alloy.*, vol. 13, no. 5, pp. 2103–2119, 2025, doi: <https://doi.org/10.1016/j.jma.2025.02.034>.
- [18] Y. Wang, M. Wei, J. Gao, J. Hu, and Y. Zhang, "Corrosion process of pure magnesium in simulated body fluid," *Mater. Lett.*, vol. 62, no. 14, pp. 2181–2184, 2008, doi: 10.1016/j.matlet.2007.11.045.
- [19] National Center for Biotechnology Information, "Density in the Periodic Table of Elements," 2025. <https://pubchem.ncbi.nlm.nih.gov/ptable/density/>
- [20] H. Hermawan, H. Alamdari, D. Mantovani, and D. Dubé, "Iron–manganese: New class of metallic degradable biomaterials prepared by powder metallurgy," *Powder Metall.*, vol. 51, no. 1, pp. 38–45, 2008, doi: 10.1179/174329008X284868.
- [21] A. Myrissa *et al.*, "In vitro and in vivo comparison of binary Mg alloys and pure Mg," *Mater. Sci. Eng. C*, vol. 61, pp. 865–874, 2016, doi: <https://doi.org/10.1016/j.msec.2015.12.064>.
- [22] Y. Zhao *et al.*, "Comparative Study on Biodegradation of Pure Iron Prepared by Microwave Sintering and Laser Melting.," *Mater. (Basel, Switzerland)*, vol. 15, no. 4, Feb. 2022, doi: 10.3390/ma15041604.
- [23] B. Jia *et al.*, "In vitro and in vivo studies of Zn-Mn biodegradable metals designed for orthopedic applications," *Acta Biomater.*, vol. 108, pp. 358–372, 2020, doi: <https://doi.org/10.1016/j.actbio.2020.03.009>.
- [24] S. Kalsi *et al.*, "Relationship between the heterogeneity in mechanical properties, bone density and composition parameters of cortical bone to design and develop bone scaffolds and implants: Analysis of bone microstructure," *Results Eng.*, vol. 24, p. 102979, 2024, doi: <https://doi.org/10.1016/j.rineng.2024.102979>.
- [25] S. Bernard, J. Schneider, P. Varga, P. Laugier, K. Raum, and Q. Grimal, "Elasticity–density and viscoelasticity–density relationships at the tibia mid-diaphysis assessed from resonant ultrasound spectroscopy measurements," *Biomech. Model. Mechanobiol.*, vol. 15, no. 1, pp. 97–109, 2016, doi: 10.1007/s10237-015-0689-6.
- [26] M. Salama, M. F. Vaz, R. Colaço, C. Santos, and M. Carmezim, "Biodegradable Iron and Porous Iron: Mechanical Properties, Degradation Behaviour, Manufacturing Routes and Biomedical Applications.," *J. Funct. Biomater.*, vol. 13, no. 2, Jun. 2022, doi: 10.3390/jfb13020072.

- [27] M. Bian *et al.*, “Improving the mechanical and corrosion properties of pure magnesium by parts-per-million-level alloying,” *Acta Mater.*, vol. 241, p. 118393, 2022, doi: <https://doi.org/10.1016/j.actamat.2022.118393>.
- [28] Q. Peng, J. Meng, Y. Li, Y. Huang, and N. Hort, “Effect of yttrium addition on lattice parameter, Young’s modulus and vacancy of magnesium,” *Mater. Sci. Eng. A*, vol. 528, no. 4, pp. 2106–2109, 2011, doi: <https://doi.org/10.1016/j.msea.2010.11.042>.
- [29] Z.-Z. Shi *et al.*, “Design biodegradable Zn alloys: Second phases and their significant influences on alloy properties.,” *Bioact. Mater.*, vol. 5, no. 2, pp. 210–218, Jun. 2020, doi: [10.1016/j.bioactmat.2020.02.010](https://doi.org/10.1016/j.bioactmat.2020.02.010).
- [30] S. Hagelstein, S. Zankovic, A. Kovacs, R. Barkhoff, and M. Seidenstuecker, “Mechanical Analysis and Corrosion Analysis of Zinc Alloys for Bioabsorbable Implants for Osteosynthesis.,” *Mater. (Basel, Switzerland)*, vol. 15, no. 2, Jan. 2022, doi: [10.3390/ma15020421](https://doi.org/10.3390/ma15020421).
- [31] F. Witte, “Reprint of: The history of biodegradable magnesium implants: A review,” *Acta Biomater.*, vol. 23, no. S, pp. S28–S40, 2015, doi: [10.1016/j.actbio.2015.07.017](https://doi.org/10.1016/j.actbio.2015.07.017).
- [32] D. Fiorentini, C. Cappadone, G. Farruggia, and C. Prata, “Magnesium: Biochemistry, Nutrition, Detection, and Social Impact of Diseases Linked to Its Deficiency.,” *Nutrients*, vol. 13, no. 4, Mar. 2021, doi: [10.3390/nu13041136](https://doi.org/10.3390/nu13041136).
- [33] D. Noviana, D. Paramitha, M. F. Ulum, and H. Hermawan, “The effect of hydrogen gas evolution of magnesium implant on the postimplantation mortality of rats,” *J. Orthop. Transl.*, vol. 5, pp. 9–15, 2016, doi: <https://doi.org/10.1016/j.jot.2015.08.003>.
- [34] O. Kurdi *et al.*, “Determination of stress shielding due to magnesium internal bone fixation,” *AIP Conf. Proc.*, vol. 2262, no. 1, p. 30018, Sep. 2020, doi: [10.1063/5.0016960](https://doi.org/10.1063/5.0016960).
- [35] O. Diard, S. Leclercq, G. Rousselier, and G. Cailletaud, “Evaluation of finite element based analysis of 3D multicrystalline aggregates plasticity: Application to crystal plasticity model identification and the study of stress and strain fields near grain boundaries,” *Int. J. Plast.*, vol. 21, no. 4, pp. 691–722, 2005, doi: <https://doi.org/10.1016/j.ijplas.2004.05.017>.
- [36] T. Shen *et al.*, “The improvement on mechanical anisotropy of AZ31 magnesium alloy sheets by multi cross-rolling process,” *J. Alloys Compd.*, vol. 963, p. 171252, 2023, doi: <https://doi.org/10.1016/j.jallcom.2023.171252>.
- [37] Y. Hollenweger and D. M. Kochmann, “An efficient temperature-dependent crystal plasticity framework for pure magnesium with emphasis on the competition between slip and twinning,” *Int. J. Plast.*, vol. 159, p. 103448, 2022, doi: <https://doi.org/10.1016/j.ijplas.2022.103448>.
- [38] J. Chen, L. Tan, X. Yu, I. P. Etim, M. Ibrahim, and K. Yang, “Mechanical properties of magnesium alloys for medical application: A review.,” *J. Mech. Behav. Biomed. Mater.*, vol. 87, pp. 68–79, Nov. 2018, doi: [10.1016/j.jmbbm.2018.07.022](https://doi.org/10.1016/j.jmbbm.2018.07.022).
- [39] K. Zhou *et al.*, “A view of magnesium alloy modification and its application in orthopedic implants,” *J. Mater. Res. Technol.*, vol. 36, pp. 1536–1561, 2025, doi: <https://doi.org/10.1016/j.jmrt.2025.03.188>.
- [40] R. A. Yokel, “The toxicology of aluminum in the brain: a review.,” *Neurotoxicology*, vol. 21, no. 5, pp. 813–828, Oct. 2000.
- [41] R. A. Yokel, *Aluminum: Properties, Presence in Food and Beverages, Fate in Humans, and Determination*, 1st ed. Elsevier Ltd., 2015. doi: [10.1016/B978-0-12-384947-2.00023-4](https://doi.org/10.1016/B978-0-12-384947-2.00023-4).

- [42] M. Haude *et al.*, “Safety and performance of the second-generation drug-eluting absorbable metal scaffold in patients with de-novo coronary artery lesions (BIOSOLVE-II): 6 month results of a prospective, multicentre, non-randomised, first-in-man trial,” *Lancet*, vol. 387, no. 10013, pp. 31–39, 2016, doi: [https://doi.org/10.1016/S0140-6736\(15\)00447-X](https://doi.org/10.1016/S0140-6736(15)00447-X).
- [43] M. . H. R. Stekker, M.; Hort, N.; Feyerabend, F.; Hoffmann, E.; Hoffmann, “Resorbable Stents Containing a Magnesium Alloy,” 2744532
- [44] J.-M. Seitz, A. Lucas, and M. Kirschner, “Magnesium-Based Compression Screws: A Novelty in the Clinical Use of Implants,” *JOM*, vol. 68, no. 4, pp. 1177–1182, 2016, doi: 10.1007/s11837-015-1773-1.
- [45] medical magnesium, “FDA Breakthrough Device designation for mm.X plate system.” <https://www.medical-magnesium.com/2023/01/11/fda-breakthrough-device-designation-for-mm-foot/> (accessed Sep. 06, 2025).
- [46] D. R. Liu, Q. Y. Sun, J. Z. Zhang, L. P. Wang, and E. J. Guo, “Numerical simulation of macrosegregation during solidification of WE43 (Mg–4.3wt-% Y–2.0wt-% Nd–0.6wt-% Gd) magnesium alloy,” *Int. J. Cast Met. Res.*, vol. 29, no. 6, pp. 376–392, 2016, doi: 10.1179/1743133615Y.0000000040.
- [47] R. Karunakaran, S. Ortgies, A. Tamayol, F. Bobaru, and M. P. Sealy, “Additive manufacturing of magnesium alloys,” *Bioact. Mater.*, vol. 5, no. 1, pp. 44–54, 2020, doi: 10.1016/j.bioactmat.2019.12.004.
- [48] J. Zhang *et al.*, “Effect of yttrium-rich misch metal on the microstructures, mechanical properties and corrosion behavior of die cast AZ91 alloy,” *J. Alloys Compd.*, vol. 471, no. 1–2, pp. 322–330, 2009, doi: 10.1016/j.jallcom.2008.03.089.
- [49] K. Luo, L. Zhang, G. Wu, W. Liu, and W. Ding, “Effect of Y and Gd content on the microstructure and mechanical properties of Mg–Y–RE alloys,” *J. Magnes. Alloy.*, vol. 7, no. 2, pp. 345–354, 2019, doi: 10.1016/j.jma.2019.03.002.
- [50] Y. Zhang *et al.*, “Influence of the amount of intermetallics on the degradation of Mg–Nd alloys under physiological conditions,” *Acta Biomater.*, vol. 121, pp. 695–712, 2021, doi: <https://doi.org/10.1016/j.actbio.2020.11.050>.
- [51] H. Ibrahim, C. Billings, M. Abdalla, A. Korra, and D. E. Anderson, “In Vivo Assessment of High-Strength and Corrosion-Controlled Magnesium-Based Bone Implants,” *Bioeng. (Basel, Switzerland)*, vol. 10, no. 7, Jul. 2023, doi: 10.3390/bioengineering10070877.
- [52] ASTM Int, “ASMT F42: Additive manufacturing — General principles — Fundamentals and vocabulary.”
- [53] ISO, “ISO/ASTM 52900:2021 Additive manufacturing — General principles — Fundamentals and vocabulary.”
- [54] K. Kanishka and B. Acherjee, “Revolutionizing manufacturing: A comprehensive overview of additive manufacturing processes, materials, developments, and challenges,” *J. Manuf. Process.*, vol. 107, pp. 574–619, 2023, doi: <https://doi.org/10.1016/j.jmapro.2023.10.024>.
- [55] M. Armstrong, H. Mehrabi, and N. Naveed, “An overview of modern metal additive manufacturing technology,” *J. Manuf. Process.*, vol. 84, pp. 1001–1029, 2022, doi: <https://doi.org/10.1016/j.jmapro.2022.10.060>.
- [56] J. Vaithilingam *et al.*, “Surface chemistry of Ti6Al4V components fabricated using selective laser melting for biomedical applications,” *Mater. Sci. Eng. C*, vol. 67, pp. 294–303, 2016, doi: 10.1016/j.msec.2016.05.054.
- [57] E. Sallica-Leva, A. L. Jardini, and J. B. Fogagnolo, “Microstructure and mechanical behavior of porous Ti–6Al–4V parts obtained by selective laser melting,” *J. Mech. Behav. Biomed. Mater.*, vol. 26, pp. 98–108, 2013.

- [58] N. Sudarmadji, J. Y. Tan, K. F. Leong, C. K. Chua, and Y. T. Loh, "Investigation of the mechanical properties and porosity relationships in selective laser-sintered polyhedral for functionally graded scaffolds," *Acta Biomater.*, vol. 7, no. 2, pp. 530–537, 2011.
- [59] Y. Wang, Y. Shen, Z. Wang, J. Yang, N. Liu, and W. Huang, "Development of highly porous titanium scaffolds by selective laser melting," *Mater. Lett.*, vol. 64, no. 6, pp. 674–676, 2010.
- [60] D. Herzog, V. Seyda, E. Wycisk, and C. Emmelmann, "Additive manufacturing of metals," *Acta Mater.*, vol. 117, pp. 371–392, 2016, doi: <https://doi.org/10.1016/j.actamat.2016.07.019>.
- [61] A. T. Clare, P. R. Chalker, S. Davies, C. J. Sutcliffe, and S. Tsopanos, "Selective laser melting of high aspect ratio 3D nickel–titanium structures two way trained for MEMS applications," *Int. J. Mech. Mater. Des.*, vol. 4, no. 2, pp. 181–187, 2008, doi: [10.1007/s10999-007-9032-4](https://doi.org/10.1007/s10999-007-9032-4).
- [62] I. Gibson, D. Rosen, and B. Stucker, *Additive Manufacturing Technologies*, vol. 9, no. 5. New York, NY: Springer New York, 2015. doi: [10.1007/978-1-4939-2113-3](https://doi.org/10.1007/978-1-4939-2113-3).
- [63] W. Zhang, M. Tong, and N. M. Harrison, "Resolution, energy and time dependency on layer scaling in finite element modelling of laser beam powder bed fusion additive manufacturing," *Addit. Manuf.*, vol. 28, pp. 610–620, 2019, doi: <https://doi.org/10.1016/j.addma.2019.05.002>.
- [64] G. V de Leon Nope, L. I. Perez-Andrade, J. Corona-Castuera, D. G. Espinosa-Arbelaez, J. Muñoz-Saldaña, and J. M. Alvarado-Orozco, "Study of volumetric energy density limitations on the IN718 mesostructure and microstructure in laser powder bed fusion process," *J. Manuf. Process.*, vol. 64, pp. 1261–1272, 2021, doi: <https://doi.org/10.1016/j.jmapro.2021.02.043>.
- [65] J. A. Pakkanen, "Designing for Additive Manufacturing-Product and Process Driven Design for Metals and Polymers," no. April, p. 134, 2018, doi: [10.6092/polito/porto/2714732](https://doi.org/10.6092/polito/porto/2714732).
- [66] J. J. Marattukalam *et al.*, "The effect of laser scanning strategies on texture, mechanical properties, and site-specific grain orientation in selective laser melted 316L SS," *Mater. Des.*, vol. 193, 2020, doi: [10.1016/j.matdes.2020.108852](https://doi.org/10.1016/j.matdes.2020.108852).
- [67] T. Delacroix *et al.*, "Influence of build characteristics and chamber oxygen concentration on powder degradation in laser powder bed fusion," *Powder Technol.*, vol. 416, p. 118231, 2023, doi: <https://doi.org/10.1016/j.powtec.2023.118231>.
- [68] Z. Zhuo, R. Ji, L. Wang, and J. Mao, "Reusability of Ti-6Al-4V powder in laser powder bed fusion: Influence on powder morphology, oxygen uptake, and mechanical properties," *J. Mater. Process. Technol.*, vol. 335, p. 118672, 2025, doi: <https://doi.org/10.1016/j.jmatprotec.2024.118672>.
- [69] R. Acharya, J. A. Sharon, and A. Staroselsky, "Prediction of microstructure in laser powder bed fusion process," *Acta Mater.*, vol. 124, pp. 360–371, 2017, doi: <https://doi.org/10.1016/j.actamat.2016.11.018>.
- [70] P. Karimi *et al.*, "Columnar-to-equiaxed grain transition in powder bed fusion via mimicking casting solidification and promoting in situ recrystallization," *Addit. Manuf.*, vol. 46, p. 102086, 2021, doi: <https://doi.org/10.1016/j.addma.2021.102086>.
- [71] G. Langelandsvik, O. M. Akselsen, T. Furu, and H. J. Roven, "Review of Aluminum Alloy Development for Wire Arc Additive Manufacturing," *Materials (Basel)*, vol. 14, no. 18, 2021, doi: [10.3390/ma14185370](https://doi.org/10.3390/ma14185370).

- [72] R. Karami, D. Butler, Y. Javadi, and S. Tamimi, "Additive manufacturing innovations: Microstructure optimisation for ultra-high silicon electrical steel components," *Mater. Charact.*, vol. 224, p. 115002, 2025, doi: <https://doi.org/10.1016/j.matchar.2025.115002>.
- [73] A. Kergaßner, J. Mergheim, and P. Steinmann, "Modelling additive manufactured materials using a crystal plasticity model," *Pamm*, vol. 16, no. 1, pp. 355–356, 2016, doi: 10.1002/pamm.201610166.
- [74] J. Liu, W. Xiong, A. Behera, S. Thompson, and A. C. To, "Mean-field polycrystal plasticity modeling with grain size and shape effects for laser additive manufactured FCC metals," *Int. J. Solids Struct.*, vol. 112, pp. 35–42, 2017, doi: 10.1016/j.ijsolstr.2017.02.024.
- [75] P. A. Hooper, "Melt pool temperature and cooling rates in laser powder bed fusion," *Addit. Manuf.*, vol. 22, no. May, pp. 548–559, 2018, doi: 10.1016/j.addma.2018.05.032.
- [76] V. Thampy *et al.*, "Subsurface Cooling Rates and Microstructural Response during Laser Based Metal Additive Manufacturing," *Sci. Rep.*, vol. 10, no. 1, pp. 1–9, 2020, doi: 10.1038/s41598-020-58598-z.
- [77] J. L. Bartlett and X. Li, "An overview of residual stresses in metal powder bed fusion," *Addit. Manuf.*, vol. 27, no. March, pp. 131–149, 2019, doi: 10.1016/j.addma.2019.02.020.
- [78] T. Mukherjee, W. Zhang, and T. DebRoy, "An improved prediction of residual stresses and distortion in additive manufacturing," *Comput. Mater. Sci.*, vol. 126, pp. 360–372, 2017, doi: 10.1016/j.commatsci.2016.10.003.
- [79] N. Nadammal *et al.*, "Effect of hatch length on the development of microstructure, texture and residual stresses in selective laser melted superalloy Inconel 718," *Mater. Des.*, vol. 134, pp. 139–150, 2017, doi: 10.1016/j.matdes.2017.08.049.
- [80] J. Robinson, I. Ashton, P. Fox, E. Jones, and C. Sutcliffe, "Determination of the effect of scan strategy on residual stress in laser powder bed fusion additive manufacturing," *Addit. Manuf.*, vol. 23, no. February, pp. 13–24, 2018, doi: 10.1016/j.addma.2018.07.001.
- [81] P. Bian, J. Shi, Y. Liu, and Y. Xie, "Influence of laser power and scanning strategy on residual stress distribution in additively manufactured 316L steel," *Opt. Laser Technol.*, vol. 132, no. August 2019, p. 106477, 2020, doi: 10.1016/j.optlastec.2020.106477.
- [82] C. T. Tsai *et al.*, "Correlating energy density induced residual stress, porosity, and mechanical property variations in directed energy deposition using neutron diffraction and imaging techniques," *J. Mater. Res. Technol.*, vol. 38, pp. 1814–1824, 2025, doi: <https://doi.org/10.1016/j.jmrt.2025.07.284>.
- [83] S. Goel *et al.*, "Residual stress determination by neutron diffraction in powder bed fusion-built Alloy 718: Influence of process parameters and post-treatment," *Mater. Des.*, vol. 195, p. 109045, 2020, doi: 10.1016/j.matdes.2020.109045.
- [84] A. Riemer and H. A. Richard, "Crack Propagation in Additive Manufactured Materials and Structures," *Procedia Struct. Integr.*, vol. 2, pp. 1229–1236, 2016, doi: 10.1016/j.prostr.2016.06.157.
- [85] M. Leary, "Surface roughness optimisation for selective laser melting (SLM): Accommodating relevant and irrelevant surfaces," *Laser Addit. Manuf. Mater. Des. Technol. Appl.*, no. 9, pp. 99–118, 2017, doi: 10.1016/B978-0-08-100433-3.00004-X.
- [86] N. Nadammal *et al.*, "Critical role of scan strategies on the development of microstructure, texture, and residual stresses during laser powder bed fusion

- additive manufacturing,” *Addit. Manuf.*, vol. 38, no. August 2020, p. 101792, 2021, doi: 10.1016/j.addma.2020.101792.
- [87] B. Mehta, *Development of high performance aluminium alloys tailored for powder bed fusion-laser beam*. 2023. [Online]. Available: [https://research.chalmers.se/en/publication/537076%0Ahttps://research.chalmers.se/publication/537076/file/537076\\_Fulltext.pdf](https://research.chalmers.se/en/publication/537076%0Ahttps://research.chalmers.se/publication/537076/file/537076_Fulltext.pdf)
- [88] M. T. Choma *et al.*, “Novel Approach To Manufacture Powders With Tailored Chemical Composition For Additive Manufacturing,” *Euro Powder Metall. 2023 Congr. Exhib. PM 2023*, no. June 2025, 2023, doi: 10.59499/EP235755976.
- [89] PubChem, “Compound Summary Magnesium Oxide.” [Online]. Available: <https://pubchem.ncbi.nlm.nih.gov/compound/Magnesium-Oxide#section=Solubility>
- [90] X. Fang *et al.*, “Additive manufacturing of high performance AZ31 magnesium alloy with full equiaxed grains: Microstructure, mechanical property, and electromechanical corrosion performance,” *J. Mater. Process. Tech.*, vol. 300, no. June 2021, p. 117430, 2022, doi: 10.1016/j.jmatprotec.2021.117430.
- [91] S. Liu *et al.*, “Influence of laser process parameters on the densification, microstructure, and mechanical properties of a selective laser melted AZ61 magnesium alloy,” *J. Alloys Compd.*, vol. 808, p. 151160, 2019, doi: 10.1016/j.jallcom.2019.06.261.
- [92] T. Kurzynowski, A. Pawlak, and I. Smolina, “The potential of SLM technology for processing magnesium alloys in aerospace industry,” *Arch. Civ. Mech. Eng.*, vol. 20, no. 1, pp. 1–13, 2020, doi: 10.1007/s43452-020-00033-1.
- [93] M. P. Sealy, R. Karunakaran, S. Ortgies, G. Madireddy, A. P. Malshe, and K. P. Rajurkar, “Reducing corrosion of additive manufactured magnesium alloys by interlayer ultrasonic peening,” *CIRP Ann.*, vol. 70, no. 1, pp. 179–182, Jan. 2021, doi: 10.1016/j.cirp.2021.04.052.
- [94] N. A. Zumdick, L. Jauer, L. C. Kersting, T. N. Kutz, J. H. Schleifenbaum, and D. Zander, “Additive manufactured WE43 magnesium: A comparative study of the microstructure and mechanical properties with those of powder extruded and as-cast WE43,” *Mater. Charact.*, vol. 147, no. November 2018, pp. 384–397, 2019, doi: 10.1016/j.matchar.2018.11.011.
- [95] C. Nilsson-Åhman, H.; Thorsson, L.; Mellin, P.; Rohimisyah, F.; Lindwall, G.; Persson, “Processing the magnesium alloy WE43 by PBF-LB,” in *EuroPM*, 2020, p. Lisbon.
- [96] V. Manakari, G. Parande, and M. Gupta, *Selective laser melting of magnesium and magnesium alloy powders: A review*, vol. 7, no. 1. 2017. doi: 10.3390/met7010002.
- [97] M. Nematollahi, A. Jahadakbar, M. J. Mahtabi, and M. Elahinia, *Additive manufacturing (AM)*, 2nd ed. Elsevier Ltd., 2019. doi: 10.1016/B978-0-08-102666-3.00012-2.
- [98] W. neng Zhang, L. zhi Wang, Z. xue Feng, and Y. ming Chen, “Research progress on selective laser melting (SLM) of magnesium alloys: A review,” *Optik (Stuttg.)*, vol. 207, no. September 2019, p. 163842, 2020, doi: 10.1016/j.ijleo.2019.163842.
- [99] N. Thirumurugan, K. P. Rao, and K. Suresh, “Cast to wrought: A multidimensional analysis on microstructure, corrosion resistance, and electrochemical behaviour of WE43 magnesium alloy,” *J. Alloys Compd.*, vol. 1031, p. 180977, 2025, doi: <https://doi.org/10.1016/j.jallcom.2025.180977>.

- [100] C. Yang, N. Gupta, H. Ding, and C. Xiang, "Effect of Microstructure on Corrosion Behavior of WE43 Magnesium Alloy in As Cast and Heat-Treated Conditions," *Metals (Basel)*, vol. 10, no. 11, 2020, doi: 10.3390/met10111552.
- [101] M. Esmaily *et al.*, "A detailed microstructural and corrosion analysis of magnesium alloy WE43 manufactured by selective laser melting," *Addit. Manuf.*, vol. 35, pp. 1–34, 2020, doi: 10.1016/j.addma.2020.101321.
- [102] H. Nilsson Åhman, F. D'Elia, P. Mellin, and C. Persson, "Microstructural Origins of the Corrosion Resistance of a Mg-Y-Nd-Zr Alloy Processed by Powder Bed Fusion – Laser Beam," *Front. Bioeng. Biotechnol.*, vol. 10, Jul. 2022, doi: 10.3389/fbioe.2022.917812.
- [103] J. Soderlind *et al.*, "Melt-Pool Dynamics and Microstructure of Mg Alloy WE43 under Laser Powder Bed Fusion Additive Manufacturing Conditions," *Crystals*, vol. 12, no. 10, 2022, doi: 10.3390/cryst12101437.
- [104] F. D'Elia, M. Hoseini-Athar, S. C. Vaddamanu, M. Ersson, P. Hedström, and C. Persson, "Influence of melting mode on melt pool dynamics and microstructure in WE43 Mg alloy: A combined computational and experimental approach," *Mater. Des.*, vol. 253, p. 113925, 2025, doi: <https://doi.org/10.1016/j.matdes.2025.113925>.
- [105] B. Yin *et al.*, "Effect of powder composition on WE43 magnesium alloy fabricated by laser powder bed fusion," *J. Mater. Res. Technol.*, vol. 32, pp. 577–588, 2024, doi: <https://doi.org/10.1016/j.jmrt.2024.07.166>.
- [106] K. Hantzsche, J. Bohlen, J. Wendt, K. U. Kainer, S. B. Yi, and D. Letzig, "Effect of rare earth additions on microstructure and texture development of magnesium alloy sheets," *Scr. Mater.*, vol. 63, no. 7, pp. 725–730, 2010, doi: <https://doi.org/10.1016/j.scriptamat.2009.12.033>.
- [107] H. M. R. Tariq, M. Ishtiaq, H.-H. Kang, U. M. Chaudry, and T.-S. Jun, "A Critical Review on the Comparative Assessment of Rare-Earth and Non-Rare-Earth Alloying in Magnesium Alloys," *Metals (Basel)*, vol. 15, no. 2, 2025, doi: 10.3390/met15020128.
- [108] H. Hyer, L. Zhou, G. Benson, B. McWilliams, K. Cho, and Y. Sohn, "Additive manufacturing of dense WE43 Mg alloy by laser powder bed fusion," *Addit. Manuf.*, vol. 33, no. October 2019, p. 101123, 2020, doi: 10.1016/j.addma.2020.101123.
- [109] S. O. Akinwamide, A. Venter, O. J. Akinribide, B. J. Babalola, A. Andrews, and P. A. Olubambi, "Residual stress impact on corrosion behaviour of hot and cold worked 2205 duplex stainless steel: A study by X-ray diffraction analysis," *Eng. Fail. Anal.*, vol. 131, p. 105913, 2022, doi: <https://doi.org/10.1016/j.engfailanal.2021.105913>.
- [110] Z. Yan, K. Wu, Z. Xiao, J. Hui, and J. Lv, "The Effect of Scanning Strategy on the Thermal Behavior and Residual Stress Distribution of Damping Alloys during Selective Laser Melting," *Materials (Basel)*, vol. 17, no. 12, 2024, doi: 10.3390/ma17122912.
- [111] V. Utyaganova *et al.*, "The effect of heat treatment of a biodegradable magnesium-based alloy produced by additive manufacturing on the product performance," *Mater. Charact.*, vol. 229, p. 115457, 2025, doi: <https://doi.org/10.1016/j.matchar.2025.115457>.
- [112] W. Xu *et al.*, "Laser powder bed fusion of WE43 magnesium alloy with superior balance of strength and ductility," *J. Magnes. Alloy.*, vol. 13, no. 3, pp. 1275–1293, 2025, doi: <https://doi.org/10.1016/j.jma.2024.03.012>.
- [113] P. Upadhyaya, S. M. U. Mhurchadha, O. J. Mccarthy, T. Kennedy, M. Celikin, and R. Raghavendra, "Enhancing the Age-Hardening Response of Laser

- Powder- Bed Fusion WE43 Alloy through Microstructural Control,” vol. 2402725, 2025, doi: 10.1002/adem.202402725.
- [114] Z. Men *et al.*, “Accurate Detection and Analysis of Pore Defects in Laser Powder Bed Fusion WE43 Magnesium Alloys,” *Micromachines*, vol. 15, no. 7, Jul. 2024, doi: 10.3390/mi15070909.
- [115] A. Koch *et al.*, “Load direction and temperature impacts on cyclic creep behavior of laser-based powder bed fusion-produced WE43 magnesium alloy,” *Addit. Manuf. Lett.*, vol. 15, p. 100316, 2025, doi: <https://doi.org/10.1016/j.addlet.2025.100316>.
- [116] F. Benn *et al.*, “Influence of surface condition on the degradation behaviour and biocompatibility of additively manufactured WE43,” *Mater. Sci. Eng. C. Mater. Biol. Appl.*, vol. 124, p. 112016, May 2021, doi: 10.1016/j.msec.2021.112016.
- [117] R. Chen, Y. Yao, J. Yong, S. Zhu, X. Xu, and N. Dai, “Pulsed laser surface texturing enhancing corrosion resistance of rare-earth WE43 magnesium alloys in simulated body fluid environment,” *J. Alloys Compd.*, vol. 1005, p. 176197, 2024, doi: <https://doi.org/10.1016/j.jallcom.2024.176197>.
- [118] A. Abel *et al.*, “PBF-LB of large-area magnesium WE43 structures surface-enhanced by plasma electrolytic oxidation,” *Prog. Addit. Manuf.*, vol. 9, no. 3, pp. 683–694, 2024, doi: 10.1007/s40964-024-00664-3.
- [119] J. Liu *et al.*, “Biodegradable magnesium alloy WE43 porous scaffolds fabricated by laser powder bed fusion for orthopedic applications: Process optimization, in vitro and in vivo investigation,” *Bioact. Mater.*, vol. 16, no. February, pp. 301–319, 2022, doi: 10.1016/j.bioactmat.2022.02.020.
- [120] T. Albaraghteh, R. Willumeit-Römer, and B. Zeller-Plumhoff, “In silico studies of magnesium-based implants: A review of the current stage and challenges,” *J. Magnes. Alloy.*, vol. 10, no. 11, pp. 2968–2996, 2022, doi: <https://doi.org/10.1016/j.jma.2022.09.029>.
- [121] K. Xie *et al.*, “Additively manufactured biodegradable porous magnesium implants for elimination of implant-related infections: An in vitro and in vivo study,” *Bioact. Mater.*, vol. 8, pp. 140–152, 2022, doi: <https://doi.org/10.1016/j.bioactmat.2021.06.032>.
- [122] M. Li *et al.*, “Microstructure, mechanical properties, corrosion resistance and cytocompatibility of WE43 Mg alloy scaffolds fabricated by laser powder bed fusion for biomedical applications,” *Mater. Sci. Eng. C*, vol. 119, p. 111623, 2021, doi: <https://doi.org/10.1016/j.msec.2020.111623>.
- [123] U. Garbe, T. Randall, C. Hughes, G. Davidson, S. Pangelis, and S. J. Kennedy, “A New Neutron Radiography / Tomography / Imaging Station DINGO at OPAL,” *Phys. Procedia*, vol. 69, pp. 27–32, 2015, doi: <https://doi.org/10.1016/j.phpro.2015.07.003>.
- [124] R. Marassi and F. Nobili, “MEASUREMENT METHODS | Structural and Chemical Properties: Scanning Electron Microscopy,” J. B. T.-E. of E. P. S. Garche, Ed. Amsterdam: Elsevier, 2009, pp. 758–768. doi: <https://doi.org/10.1016/B978-044452745-5.00071-X>.
- [125] H. M. Rietveld, “A profile refinement method for nuclear and magnetic structures,” *J. Appl. Crystallogr.*, vol. 2, no. 2, pp. 65–71, Jun. 1969, doi: 10.1107/S0021889869006558.
- [126] J. Rodriguez-Carvajal, “Recent developments of the program FULLPROF, commission on powder diffraction,” *IUCr Newsl.*, vol. 26, 2001.
- [127] A. Coelho, “TOPAS Academic.” 2004. [Online]. Available: <http://www.topas-academic.net>

- [128] A. Belsky, M. Hellenbrandt, V. . Karen, and P. Luksch, “New Developments in the Inorganic Crystal Structure Database (ICDS): Accessibility in support of materials research and design,” *Acta crystallogr. B*, no. 58, pp. 364–369, 2002.
- [129] ASTM Int, “ASTM E8/E8M-13a, Standard test methods for tension testing of metallic materials.” 2013.
- [130] C. Öhman-Mägi, O. Holub, D. Wu, R. M. Hall, and C. Persson, “Density and mechanical properties of vertebral trabecular bone-A review.,” *JOR spine*, vol. 4, no. 4, p. e1176, Dec. 2021, doi: 10.1002/jsp2.1176.
- [131] J. S. Nyman, H. Leng, X. N. Dong, and X. Wang, “Differences in the mechanical behavior of cortical bone between compression and tension when subjected to progressive loading.,” *J. Mech. Behav. Biomed. Mater.*, vol. 2, no. 6, pp. 613–619, Dec. 2009, doi: 10.1016/j.jmbbm.2008.11.008.
- [132] H. N. Åhman, L. Larsson, C. Wahman, P. Mellin, F. D’Elia, and C. Persson, “Higher laser power improves strength but reduces corrosion resistance of Mg WE43 processed by powder bed fusion,” *Mater. Today Commun.*, vol. 39, p. 108979, 2024, doi: <https://doi.org/10.1016/j.mtcomm.2024.108979>.
- [133] H. Nilsson-Åhman *et al.*, “Nilsson-Åhman, Hanna and De Berardinis, Niccolò and Larsson, Lisa and Rothkranz, Leon and Mellin, Pelle and D’Elia, Francesco and Hulsart-Billström, Gry and Persson, Cecilia, Laser hatch distance can tune corrosion behavior and mechanical properties while,” *SSRN J. Pre-print*, 2025.
- [134] L. Larsson, F. D’Elia, M. Sahlberg, and C. Persson, “Leveraging laser powder bed fusion to alter texture and mechanical properties of magnesium alloy WE43,” *Mater. Des.*, vol. 256, p. 114299, 2025, doi: <https://doi.org/10.1016/j.matdes.2025.114299>.
- [135] G. Li *et al.*, “Investigation into the effect of energy density on densification, surface roughness and loss of alloying elements of 7075 aluminium alloy processed by laser powder bed fusion,” *Opt. Laser Technol.*, vol. 147, p. 107621, 2022, doi: <https://doi.org/10.1016/j.optlastec.2021.107621>.
- [136] H. S. Jiang *et al.*, “Materials Science & Engineering A Microstructure and mechanical properties of WE43 magnesium alloy fabricated by direct-chill casting,” vol. 684, no. August 2016, pp. 158–164, 2017, doi: 10.1016/j.msea.2016.11.009.
- [137] X. Zhang, G. Yuan, L. Mao, J. Niu, and W. Ding, “Biocorrosion properties of as-extruded Mg–Nd–Zn–Zr alloy compared with commercial AZ31 and WE43 alloys,” *Mater. Lett.*, vol. 66, no. 1, pp. 209–211, 2012, doi: <https://doi.org/10.1016/j.matlet.2011.08.079>.
- [138] Y. Shi, K. Guo, H. Shi, X. Huang, B. Yang, and J. Sun, “Effects of process parameters on microstructure properties of WE43 magnesium alloy by selective laser melting,” *Mater. Today Commun.*, vol. 39, p. 109151, 2024, doi: <https://doi.org/10.1016/j.mtcomm.2024.109151>.
- [139] G. Pietro Cavaliere, V. Shtender, P. Mellin, C. Persson, and F. D’Elia, “Powder reuse in powder bed fusion-laser beam of WE43 magnesium alloy: towards sustainable manufacturing of biodegradable implants,” *J. Mater. Res. Technol.*, 2025, doi: <https://doi.org/10.1016/j.jmrt.2025.08.261>.
- [140] T. Rzychoń, B. Dybowski, A. Gryc, and M. Dudek, “Mechanical Properties and Microstructure of WE43 Magnesium Matrix Composite Reinforced SiC Particles,” vol. 15, no. 1, p. 101, 2015.
- [141] Y. H. Kang, Z. H. Huang, S. C. Wang, H. Yan, R. S. Chen, and J. C. Huang, “Effect of pre-deformation on microstructure and mechanical properties of WE43 magnesium alloy II: Aging at 250 and 300 °C,” *J. Magnes. Alloy.*, vol. 8, no. 1, pp. 103–110, 2020, doi: <https://doi.org/10.1016/j.jma.2019.11.012>.

- [142] P. Pant *et al.*, “Mapping of residual stresses in as-built Inconel 718 fabricated by laser powder bed fusion: A neutron diffraction study of build orientation influence on residual stresses,” *Addit. Manuf.*, vol. 36, p. 101501, 2020, doi: <https://doi.org/10.1016/j.addma.2020.101501>.
- [143] A. Kopp *et al.*, “Influence of design and postprocessing parameters on the degradation behavior and mechanical properties of additively manufactured magnesium scaffolds,” *Acta Biomater.*, vol. 98, pp. 23–35, 2019, doi: [10.1016/j.actbio.2019.04.012](https://doi.org/10.1016/j.actbio.2019.04.012).
- [144] H. Gao *et al.*, “Enhancement of epitaxial growth and mechanical properties of DZ125 superalloy fabricated by defocused-laser powder bed fusion via rotation angle optimization,” *Mater. Sci. Eng. A*, vol. 930, p. 148113, 2025, doi: <https://doi.org/10.1016/j.msea.2025.148113>.
- [145] W. Frieden Templeton, S. Hinnebusch, S. T. Strayer, A. C. To, P. C. Pistorius, and S. P. Narra, “A mechanistic explanation of shrinkage porosity in laser powder bed fusion additive manufacturing,” *Acta Mater.*, vol. 266, p. 119632, 2024, doi: <https://doi.org/10.1016/j.actamat.2023.119632>.
- [146] K. Tosha, “Influence of Residual Stresses on the Hardness Number in the Affected Layer Produced by Shot Peening,” *2nd Asia-Pacific Forum Precis. Surf. Finish. Deburring Technol. Asia-Pacific Forum Precis. Surf. Finish. Deburring Technol.*, pp. 48–54, 2002, [Online]. Available: <http://citeseerx.ist.psu.edu/viewdoc/download?doi=10.1.1.600.5688&rep=rep1&type=pdf>

# Acta Universitatis Upsaliensis

*Digital Comprehensive Summaries of Uppsala Dissertations from the Faculty of Science and Technology 2601*

Editor: The Dean of the Faculty of Science and Technology

A doctoral dissertation from the Faculty of Science and Technology, Uppsala University, is usually a summary of a number of papers. A few copies of the complete dissertation are kept at major Swedish research libraries, while the summary alone is distributed internationally through the series Digital Comprehensive Summaries of Uppsala Dissertations from the Faculty of Science and Technology. (Prior to January, 2005, the series was published under the title “Comprehensive Summaries of Uppsala Dissertations from the Faculty of Science and Technology”.)

Distribution: [publications.uu.se](http://publications.uu.se)  
urn:nbn:se:uu:diva-569726



ACTA UNIVERSITATIS  
UPSALIENSIS  
2025